JOHANNES KEPLER
UNIVERSITÄT LINZ | JKU

TNF

Technisch-Naturwissenschaftliche
Fakultät

Electrochemical doping of organic field-effect transistors to improve contact resistances

DIPLOMARBEIT

zur Erlangung des akademischen Grades

Diplomingenieur

im Diplomstudium

Technische Physik

Eingereicht von:
Stefan Schaur

Angefertigt am:
Institut für Physikalische Chemie

Beurteilung:
o.Univ.-Prof. Dr. Niyazi Serdar Sariciftci

Betreuung:
DI Philipp Stadler

Linz, Juni 2010

Eidesstattliche Erklärung

Ich erkläre an Eides statt, dass ich die vorliegende Diplomarbeit selbstständig und ohne fremde Hilfe verfasst, andere als die angegebenen Quellen und Hilfsmittel nicht benutzt bzw. die wörtlich oder sinngemäß entnommenen Stellen als solche kenntlich gemacht habe.

Linz, im Juni 2010

Stefan Schaur

Acknowledgements

First of all I want to thank my family, especially my parents, for all their support and motivation during the years of my studies.

Special thanks go to my mentors, Philipp Stadler, who has taught me a lot about chemistry and organic transistors, and Beatriz Meana-Esteban, for her patience in introducing a physicist to the world of electrochemistry. Their enthusiasm for this work has always been one of the biggest motivations for me.

Further I want to thank Prof. Dr. N. S. Sariciftci for his advice and for making this work possible, and Dr. Helmut Neugebauer for his advice, especially concerning electrochemistry.

I also want to thank all the people at this institute for their time, help, advice and inspiring discussions, especially the people in my office, namely Alberto Montaigne Ramil, Jacek Gasiorowski, Mamatimin Abbas and Philipp Stadler.

Finally I would like to say “Thank you!” to my fellow students and friends for all the support, motivation and good times in all the years!

Abstract

Pentacene is an organic semiconductor known to exhibit ambipolar transport in organic field-effect transistors (OFET). Therefore first the redox properties of pentacene by electrochemical methods, namely cyclic voltammetry and electrochemical voltage spectroscopy, were studied. To get a more detailed insight into the material properties, *in-situ* UV-visible (UV-VIS) and FTIR-attenuated total reflection spectroscopy (FTIR-ATR) measurements were conducted.

It was found that pentacene can be reversibly oxidized and reduced, corresponding to electrochemical *p*- and *n*-doping of the material, and the idea originated to apply this knowledge to a working transistor in order to improve its performance.

The spectroscopic data suggests that the material responds very differently to each of the doping processes. As pentacene is primarily used as a *p*-type semiconductor, the focus of this work was put on the influence of the *p*-doping process on the transistor performance.

By electrochemically *p*-doping the pentacene in the vicinity of the source and drain contacts, the injection barrier for positive charge carriers (holes) should decrease. This effect was indeed measured by comparing the contact resistance of the transistors before and after the doping process, leading to an improvement of the device performance.

Zusammenfassung

Pentacen ist ein organischer Halbleiter, welcher bekannt ist für seine ambipolaren Eigenschaften in organischen Feldeffekttransistoren. Deshalb wurden die Redoxeigenschaften mit elektrochemischen Methoden, wie zyklischer Voltametrie und “electrochemical voltage spectroscopy” untersucht. Zum besseren Verständnis der Materialeigenschaften von Pentacen wurden weiters *in-situ* UV/VIS- und FTIR-ATR-Spektroskopiemessungen durchgeführt.

Das Ergebnis zeigt, dass Pentacen reversibel oxidiert und reduziert werden kann, was einer *p*- beziehungsweise *n*-Dotierung des Materials entspricht. Dieses Wissen sollte nun zur Verbesserung der Funktionsweise eines Transistors angewandt werden. Da Pentacen primär als *p*-Halbleiter verwendet wird, liegt der Fokus dieser Diplomarbeit auf der Erforschung der Auswirkungen der *p*-Dotierung auf die Transistoreigenschaften.

Durch elektrochemisches *p*-Dotieren von Pentacen in der Kontaktregion der Source- und Drain-Kontake sollte die Löcherinjektion vereinfacht werden. Dieser Effekt konnte mithilfe von Kontaktwiderstandsmessungen vor beziehungsweise nach dem Dotiervorgang bestätigt werden, und führte zu einer Verbesserung der Transistoreigenschaften.

Contents

Part I

Introduction

1 Motivation

Pentacene is an organic semiconductor known to exhibit ambipolar transport in organic field-effect transistors [1, 2]. Therefore it was interesting if this would also be reflected in the electrochemical properties of the material, namely if it can be reversibly *p*- and *n*-doped.

Furthermore the bandgap of the material can be determined straightforward from the electrochemical measurements, without having to use any other sophisticated method known from the literature like UV photoemission spectroscopy (UPS) or scanning-tunneling spectroscopy (STS). This provides knowledge about the electronic levels of pentacene, and can help to choose the correct metals for contacting it in a transistor.

Though ambipolar, when used in an organic field-effect transistor the device performance of pentacene in the *p*- and the *n*-side is not the same. Therefore, to get a more detailed insight into the material properties, spectroscopic methods can be applied to observe changes during the electrochemical process.

With the knowledge obtained from the measurements mentioned above, it was time to think about an application in an actual working transistor. From the literature it was known that chemical doping of organic semiconductors can lead to a decrease in the contact resistance of field-effect transistors [3, 4]. Therefore the idea was to show the same effect by electrochemical doping, which can be even more precisely controlled than chemical doping.

Thus electrochemistry was used to dope the pentacene in the vicinity of the source and drain contacts of a transistor, which should lead to a decrease of the injection barrier for charge carriers. If so, this would be resembled in a decrease of the contact resistance and an improvement of the transistor behaviour.

2 Organic semiconductors

2.1 Introduction

Carbon, an element of column IV of the periodic table, is the main building unit of organic polymers. It has four valence electrons, and may exist in either sp, sp^2 or sp^3 hybridized form. Most well-known in everyday life are the sp^3 hybrids, or so-called saturated compounds, where all four valence electrons form covalent σ bonds with neighbouring (carbon) atoms. The energy difference between the bonding and antibonding σ bonds is high, therefore these polymers are typically insulators and transparent in the visible spectral range [5, 6]. The materials they form are what we usually call "plastics", like they are used for plastic bags or bottles (most widely used is polyethene, also called polyethylene, PE, with an annual production of almost 80 million tons [7, p. 32]).

Concerning electronic properties, the situation is much more interesting for conjugated materials. They are sp^2 hybridized, with three strong σ bonds and a p_z orbital, which is orthogonal to the sigma bonds, and has formally one unpaired electron. While the σ bonds account for the rigidity of the material, the p_z orbitals of neighbouring atoms overlap and form a π bond, where the energy difference between bonding (π) and antibonding (π^*) states (also called *highest occupied* and *lowest unoccupied molecular orbitals* - HOMO and LUMO) is less than between the σ and σ^* bonds (see Figure 2.1 a) for an illustration of this concept). For larger molecules the electrons in the π orbitals are delocalized along the backbone of the polymer and form a π system which extends over the whole molecule.

As a large number of carbon atoms are brought together in the polymer, their individual energy levels (π/π^*) become so closely spaced that they cannot be distinguished any more, leading to the formation of *energy bands*. This is explained by the Hückel theory: The orbital energies for a carbon chain with n atoms are confined to a certain range. With increasing n, the increasing number of energy levels are getting more closely spaced, as do the HOMO and LUMO levels. For a very large number of atoms the energy difference between two states approaches zero, leading to the formation of one continuos band of energy levels.

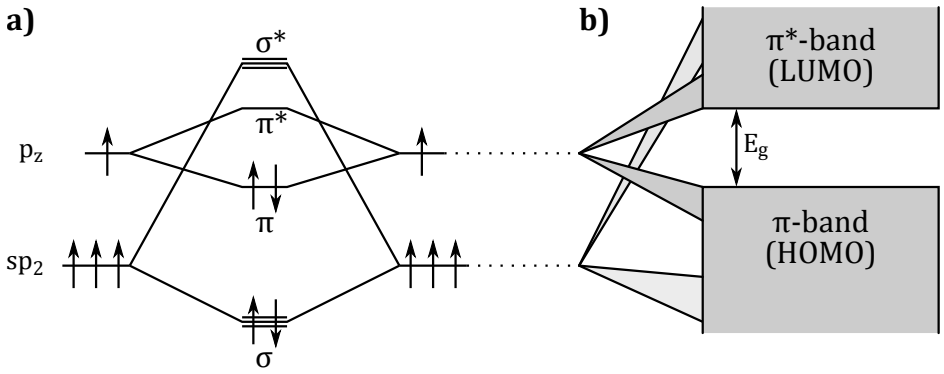

Figure 2.1: Energy scheme for C_2H_2 (a) and for a large number of carbon atoms in a conjugated polymer (b)

From the above considerations the HOMO and LUMO effectively merge, forming a half-filled band which by the band theory of solids should lead to metallic conductivity (see also Figure 2.3). How can semiconducting behaviour be explained in this picture?

The metallic behaviour is only the case for molecules where all bonds in the backbone are of equal length. As shown by Peierls in 1955 [8, chap. 5.3], a typical effect in such a material is that they tend to distort spontaneously, forming alternating single- and double-bonds, as this form is energetically more favorable. This effect is called dimerization, and the resulting bond-alternating structure is characteristic for conjugated materials. The dimerization creates an energy gap at the Fermi level which splits the expected metallic band into an occupied and an unoccupied band, seperated by the gap energy E_g, and therefore forming a *semiconducting material* [5, 9], as sketched in Figure 2.1 b). The occupied band may be referred to as the HOMO, valence band (VB) or π-orbital, and the unoccupied band is called LUMO, conduction band (CB) or π^*-orbital.

Organic semiconductors can be classified as *polymers* and *small molecules*. In this work pentacene was used as a semiconductor, as further described in Sec. 5.4. Pentacene is a small molecule from the group of oligoacenes, consisting of five aligned condensed benzene rings, and is widely used for preparation of *p*-type organic field-effect transistors. While pentacene can only be deposited by vacuum evaporation, a functionalized form of pentacene named triisopropylsilylethynyl (TIPS) pentacene is soluble in common organic solvents [10]. Other famous small molecules are for example phtalocyanines, for which semiconductivity was reported as early as 1948 [11], or the fullerene C_{60}, which is an *n*-type semiconductor. Representatives for conducting polymers are for example polyacetylene or polythiophene. The structures of these semiconductors are shown in Figure 2.2.

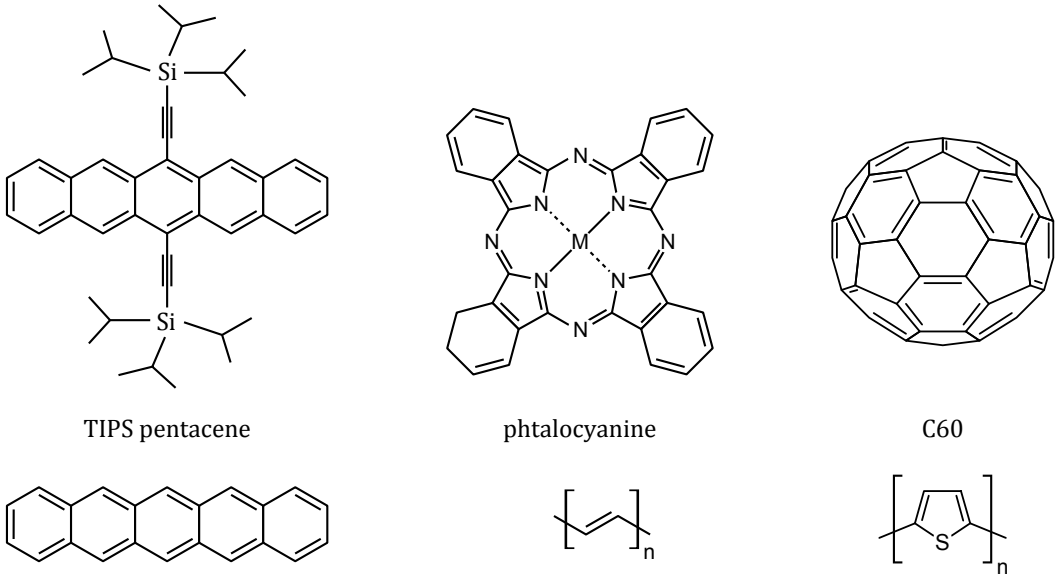

TIPS pentacene | phtalocyanine | C60

pentacene | polyacetylene | polythiophene

Figure 2.2: Structural diagrams of TIPS pentacene, phtalocyanine (where M is a metal atom), C_{60} and pentacene, and molecular structures of *trans*-polyacetylene and polythiophene

2.2 Charge transport mechanisms

2.2.1 Band-like transport

From the theory of inorganic, crystalline solids the mechanism of band transport is well known, explaining the behaviour of metals and semiconductors [12, chap. 3]. The distribution of charge carriers in the bands of the solid are determined by the Fermi-Dirac distribution, which states that at $T = 0$ all energy states are occupied up to a level E_F, the so-called Fermi energy.

From the position of the Fermi level, solids can be distinguished into metals, insulators and semiconductors, as depicted in Figure 2.3. If the Fermi level lies within a band, it is partly filled and partly empty, leading to metallic behaviour. If the Fermi level lies in the gap between two bands, the highest occupied band will be completely filled, and the other one empty. No free charge carriers are present, therefore this material is called an insulator. If the gap between the two bands is rather small however, electrons may be thermally activated from the valence band into the conduction band at $T > 0$. This highly temperature dependent conductivity is specific for an intrinsic semiconductor.

One example of the behaviour of "band transport" in organic semiconductors was found in highly pure crystals of acenes by Karl et al. [13]. However the exact nature of this behaviour is still under discussion [6, chap. 2.2].

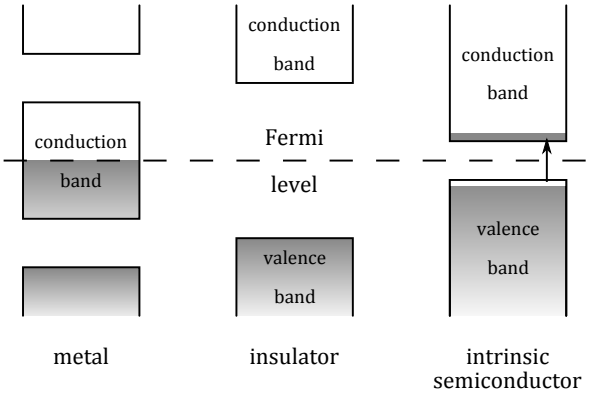

Figure 2.3: Band diagrams of a metal (at $T = 0$), an insulator and an intrinsic semiconductor (at $T > 0$), with the Fermi energy depicted as the dashed line

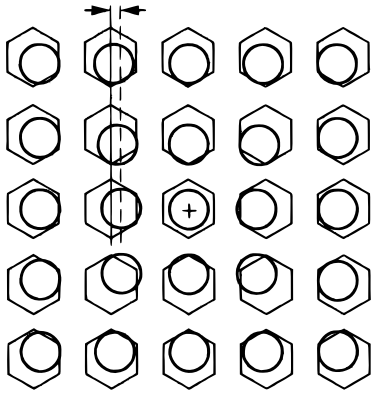

Figure 2.4: Schematic representation of a polaron in a solid symbolized by benzene rings, with a positiv charge on the center molecule, and the π electrons (circles) of the other molecules shifting towards the center charge relatively to their atomic nuclei (hexagons)

2.2.2 Polaron transport

According to the model of "band transport", the charge carriers move freely in the solid, driven by an external field, and damped by collisions, mainly with lattice vibrations, so-called phonons. One main issue not taken into account in this model are polarization effects occurring in organic semiconductors, described in the following.

If a charge carrier resides in a molecule site, it tends to polarize its surroundings. This effect is illustrated in Figure 2.4. The resulting polarization cloud moves with the charge carrier as it travels through the semiconductor. This combined movement creates a new species called a *polaron*.

On a molecular level the polaron can be viewed as an extra charge associated with a local geometrical relaxation of the lattice, as illustrated in Figure 2.5 for the example of poly(*p*-phenylenevinylene), where a positive charge is sited at a domain boundary. This lattice distortion effectively localizes the charge. The localized electronic state associated with the polaron lies in the gap between π and π^* levels [14], close to the respective main transport band, which is the HOMO level for the case of a positive polaron. Two theories describing the transport properties of such localized charges will be shortly presented in the following. Both account for the temperature and gate voltage dependence of mobility usually found in organic semiconductors.

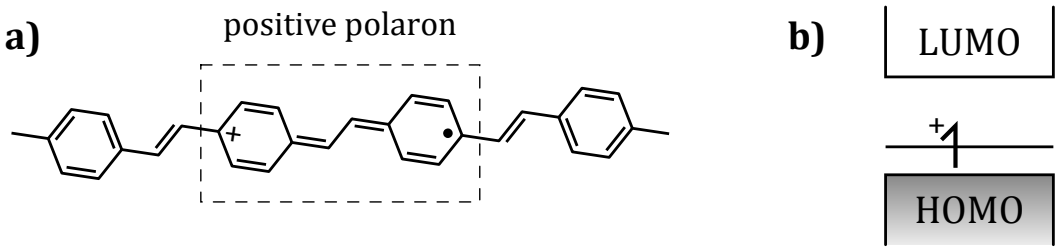

Figure 2.5: Schematic picture of a positive polaron in poly(*p*-phenylenevinylene) (a), and the corresponding band diagram, with the the single occupied low lying gap state (b)

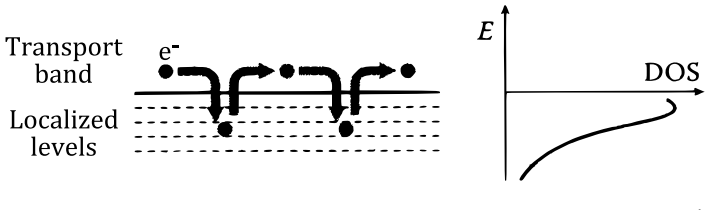

Figure 2.6: Principle of charge transport as described by the MTR model (left) with a schematic energy distribution of localized trap states (right) (from: [6, chap. 2.2])

The MTR model In the model of multiple trapping and thermal release (MTR) an energy distribution of localized trap states near the transport band is assumed, as described by Horowitz et al. [15]. The assumption of a transport band already suggests that this model is more suitable for well-ordered organic systems.

The description of the transport properties rests on two mechanisms (see Figure 2.6): (i) charges are released by thermal activation from the trap state into the delocalized transport band and (ii) when arriving at a new trap state they are recaptured with a probability close to one. From the first point it is clear that the mobility is temperature dependent, as with increasing temperature more charge carriers are activated and contribute to the transport. An increase in mobility with increasing gate voltage is explained by a shift of the Fermi level within the region of the energy distributed trap states. As the Fermi level moves closer to the transport band edge, more and more trap states of higher energy get filled, thus reducing the energy difference between localized and delocalized states, and charge carriers are more easily thermally activated.

The VRH model The model of variable range hopping (VRH) is useful to describe the transport properties in disordered materials. As described by Vissenberg and Matters [16], charge carriers are assumed to be strongly localized, described by an exponential density of states. Transport is described by a thermally activated tunneling between these localized

states, called *hopping*. The hopping rate is of the form of a generalized Miller-Abrahams [17] type:

$$\nu = \nu_0 \cdot e^{-2 \cdot R_{ij} \cdot \alpha} \cdot e^{-\Delta E \cdot \delta(E)/(kT)}$$

The first term describes the overlap of the electronic wave functions of the trap sites *i* and *j* as a product of their distance *R* times an overlap parameter α. The second term accounts for the activation energy ΔE necessary to hop upwards in energy to another trap state, times a factor $\delta(E)$ describing the occupational probabilities of the sites *i* and *j*.

From this ansatz it is also clear why the name "variable" range hopping is used: it is equally probable for a charge carrier to make a long distance hop associated with a small energy change, or a small hop when a high activation energy is necessary. Like in the MTR model the temperature dependence originates from the thermal activation mechanism. Additionally, as shown by N. F. Mott [18], the thermal activated hopping at low temperatures deviates from the form $\exp(-\Delta E/(kT))$, and the conductivity follows a law of $\sigma = A \cdot \exp(-B/T^{\frac{1}{4}})$ instead.

Again similar to the MTR model, an increase of gate voltage leads to the occupation of higher energetical localized states, which on average will require less activation energy to hop to a neighbouring site.

2.3 Doping of organic semiconductors

Reversible charge injection into a conjugated material is commonly referred to as *doping*. Reports by Shirakawa et al. [19, 20] showed that by chemically doping *trans*-polyacetylene its conductivity could be changed by eleven orders of magnitude in the full range from an insulator to a conducting metal. However one should not confuse the "doping" of conjugated polymers with the doping which is known from the silicon industry. As for silicon, a dopant atom is put into a position in the silicon lattice, replacing the lattice atom. In conjugated materials on the other hand doping is a mere *charge transfer process*, during which the doped material gets partially oxidized (*p*-doped) or reduced (*n*-doped). Four possible methods for achieving this charge transfer are shown in Figure 2.7, namely chemical, electrochemical, interfacial and photoinduced doping, where the former 3 will be described shortly in the following.

Chemical doping was the first doping mechanism to be discovered. As described in [20], the polyacetylene films were "treated with the vapor of the dopant at room temperature, *in vacuo*, for 3–4 hours". Controlled amounts of chlorine, bromine or iodine, as well as arsenic pentafluoride served as electron acceptors. While chemical doping provides an efficient and straightforward way of doping, it is difficult to obtain an intermediate state of doping, and the polymer is usually fully doped.

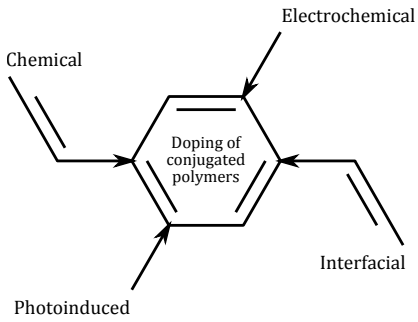

Figure 2.7: Four different doping mechanisms used on conjugated polymers

A more elegant and well controllable process is offered by *electrochemical doping*. This method is conducted in an electrochemical cell, and the polymer acting as the working electrode is either oxidized (electrons are taken out of the material) or reduced (electrons are put into the material), until an electrochemical equilibrium is reached. To keep electroneutrality in the material, ions from the electrolyte diffuse into the polymer. By choosing a specific potential value, the doping level of the polymer can be precisely controlled. The charge transfer process is illustrated by the following example [14], using a $\mathrm{TBA}^+(\mathrm{PF}_6^-)$ electrolyte:

- Oxidation (p-doping)

$$(\pi\text{-polymer}) + \left[\mathrm{TBA}^+(\mathrm{PF}_6^-)\right]_{solv} \quad \rightarrow \quad \left[(\pi\text{-polymer})^{x+}(\mathrm{PF}_6^-)_x\right] + x(\mathrm{TBA}^+) + xe^-$$

- Reduction (n-doping)

$$(\pi\text{-polymer}) + xe^- + \left[\mathrm{TBA}^+(\mathrm{PF}_6^-)\right]_{solv} \quad \rightarrow \quad \left[(\pi\text{-polymer})^{x-}(\mathrm{TBA}^+)_x\right] + x(PF_6^-)$$

Yet another method is the so-called *interfacial doping*. Here the charges can be injected from metal contacts into the polymer. Depending on the sign of the applied voltage, the following mechanisms are possible:

- electron injection – n-doping

$$(\pi\text{-polymer}) + xe^- \quad \rightarrow \quad (\pi\text{-polymer})^{x-}$$

- hole injection – p-doping

$$(\pi\text{-polymer}) - xe^- \quad \rightarrow \quad (\pi\text{-polymer})^{x+}$$

This doping effect takes place in organic field-effect transistors (OFETs) or polymer light-emitting diodes, and is further described in Sec. 4.3. It is important to note that for interfacial doping, in contrast to chemical and electrochemical doping, no counterions are present in the polymer.

3 Electrochemistry and spectroscopy

3.1 Electrochemistry

In many electrochemical techniques the current-potential curves for the electrode reactions are measured and studied. These techniques are combined under the term *voltammetry*, and the current-potential curves are called voltammograms. A typical setup for a voltammetric measurement is shown in Figure 3.1. A potentiostat, supported by a voltage source, applies a potential between the working (WE) and the counter electrode (CE). The name working electrode is due to the fact that the process under study occurs there. A high-impedance reference electrode (RE) is used to measure and control the potential precisely. The resulting current through the electrochemical cell is then measured and recorded, together with the potential.

While the working and counter electrode are usually composed of inert materials which do not participate in the redox reaction but only provide a surface, the situation is more difficult for the reference electrode. It must feature a stable and reproducible potential, to which other potentials and potential differences can be related. In aqueous solutions, the so-called normal hydrogen electode (NHE) is used. However in non-aqueous solutions, which will be treated here, this is not applicable, as water may leak into the system from the NHE. Also, there is the danger of undefined liquid-liquid junction potentials between cell and electrode compartment. Instead in our setup a silver-silver chloride (Ag/AgCl) quasi-reference electrode (QRE) was used, and platinum (Pt) was used for the working and counter electrodes. To be able to compare the measurements performed with the Ag/AgCl QRE to measurements obtained with other reference electrodes, a reference redox system is measured. A cyclic voltammogram of the oxidation of ferrocene to ferrocenium (Fc/Fc^{+}) is recorded, and the redox potential of the redox couple is used as a reference value for all other measurements in the system (see “cyclic voltammetry” below for details).

Besides the electrodes the choice of electrolyte solution is of importance. For experiments conducted with non-aqueous solvents, it is important to work under inert atmosphere free of moisture. One main criterion for the electrolyte is its stability within the potential range that is necessary for the analyzation of the investigated material. Therefore so-called “potential win-

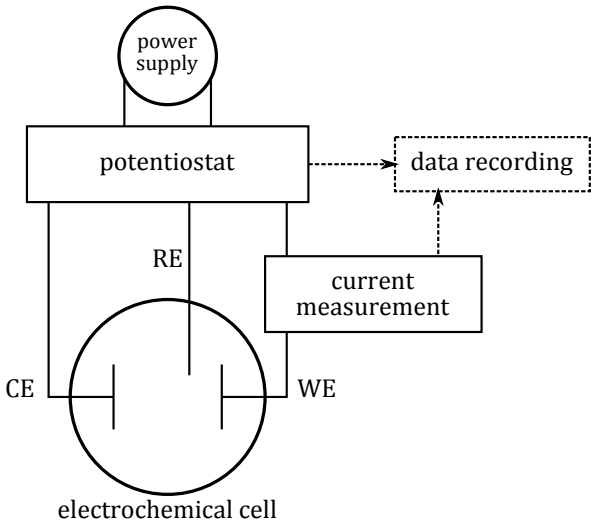

Figure 3.1: Schematic of an electrochemical setup, with the labels for counter electrode (CE), reference electrode (RE) and working electrode (WE)

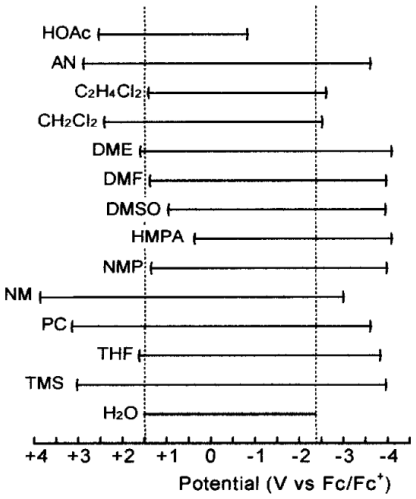

Figure 3.2: Potential windows for various solvents, measured versus the ferrocene/ferrocenium couple (from: [21, chap. 4])

dows" are defined for various solvents, as shown in Figure 3.2. The potential window indicates at which potentials the solvent itself gets oxidized or reduced, therefore making any further analyzation of material impossible. To improve the conductivity of the solution, a *supporting electrolyte* is added to the solvent. Its main requirements are (i) to be soluble in the used solvent, (ii) to dissociate readily into ions to give conductivity to the solution, and (iii) to support a wide potential window as well.

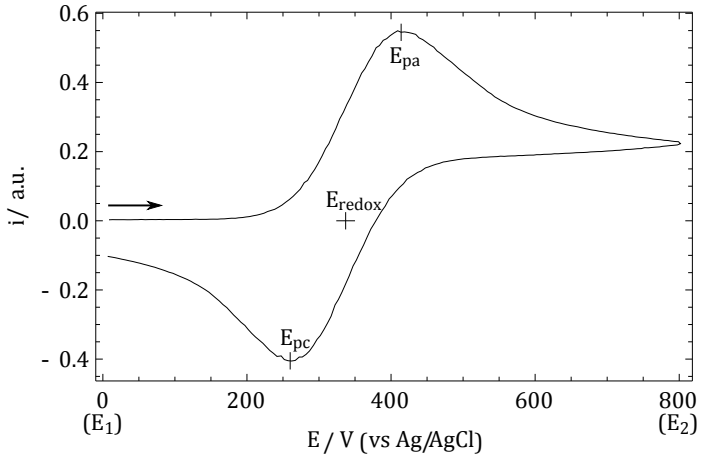

Figure 3.3: Typical cyclic voltammogram for the Fc/Fc^+ couple, as recorded in 0.1 M $TBAPF_6$-ACN

As described in the experimental section on page 37, acetonitrile (ACN) was chosen as a solvent for the experiments in this work, together with a tetrabutylammonium hexafluorophosphate ($TBAPF_6$) salt as supporting electrolyte. The potential window of ACN is indicated in Figure 3.2 as "AN".

Cyclic voltammetry With the appropriate working setup, the material of interest can be investigated. Cyclic voltammetry (CV) was chosen as the electrochemical technique to study the redox reactions of pentacene. Here, the applied potential is scanned linearly from a value E_1 to a value E_2 and back to E_1. When studying the oxidation process of ferrocene for example, the potential is first scanned to the positive direction, and the anodic peak is observed upon oxidation of the material. When scanning back, the cathodic peak is observed, due to the re-reduction of the material. The cyclic voltammogram for this process is shown in Figure 3.3. The redox potential $E_{redox} = (E_{pa} + E_{pc})/2$ is derived from the position of the anodic peak (E_{pa}) and the cathodic peak (E_{pc}) and serves as a reference value for other measurements.

3.2 Spectroelectrochemistry

While cyclic voltammetry can give information about the redox properties of a material, it can not give insight into what happens at a molecular level at the working electrode. Therefore electrochemistry is often combined with other, non-electrochemical methods. For this work two such methods have been used, namely absorption spectroscopy in the UV-visible (UV-VIS) and the infrared regime, using the Attenuated Reflection Mode (FTIR-ATR). As the absorption

spectra are recorded *during* the electrochemical process, the methods are termed *in-situ* techniques.

Explaining both methods here would go beyond the scope of this work, therefore only references to detailed information in the literature are given. The experimental setups are then described in further detail in chapter 6. For information about UV-visible measurements see "Instrumental methods in electrochemistry" [22, chap. 10]. An overview of *in-situ* infrared spectroscopic methods is given in "Advanced Functional Molecules and Polymers" [23, chap. 6].

4 Organic field-effect transistors

4.1 Introduction

The principle of the field-effect transistor (FET) was first proposed by Lilienfeld in a patent in 1930 [24]. It took then thirty years until the first silicon-based metal-oxide-semiconductor FET (MOSFET) was fabricated by Kahng and Atalla in 1960 [25]. Nowadays, MOSFETs are mainly produced from single-crystalline silicon due to its excellent oxide-forming properties, and are probably the most widely used device in modern microelectronics. A more general term for devices which do not use silicon dioxide as a gate insulator but have the same device structure as the MOSFET is *metal-insulator-semiconductor field-effect transistor* (MISFET).

The concept of the thin film transistor (TFT) was first introduced in 1962 by Weimer [26]. This type of device architecture is especially useful for low conductivity materials, and is currently widely used in amorphous silicon transistors [27]. Replacing the inorganic silicon by an organic semiconductor the device structure of an organic field-effect transistor (OFET) is obtained. This kind of electronic device was first reported by Koezuka and co-workers in 1987 [28] where they used a conducting polymer called polythiophene as the active material.

4.2 Transistor architectures

The structures of two kinds of FET are illustrated in Figure 4.1. In 4.1 a), an inorganic p-channel enhancement mode MOSFET is shown. Two metals, called *source* and *drain*, form ohmic contacts to highly *p*-doped areas in an *n*-type substrate, whereas the third contact, the *gate*, is insulated from the substrate by an oxide layer. By applying a potential to the gate electrode, the charge carrier density at the insulator-semiconductor interface can be controlled, and three different operating regimes, namely accumulation, depletion and inversion, can be distinguished, as depicted in the energy-band diagrams in Figure 4.2 [12].

If a positive potential is applied to the gate, the bands bend downwards. The conduction-band edge is closer to the Fermi level at the oxide-semiconductor interface than in the bulk material, and an *accumulation* layer of electrons is induced at the interface (4.2 a)). For a mod-

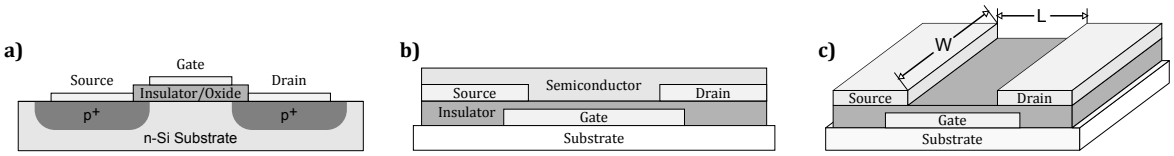

Figure 4.1: Sketch of a) a silicon *p*-channel enhancement mode MOSFET; b) an organic field-effect transistor and c) a three-dimensional sketch of the same OFET transistor depicting *L* and *W*, where the semiconductor layer is not shown

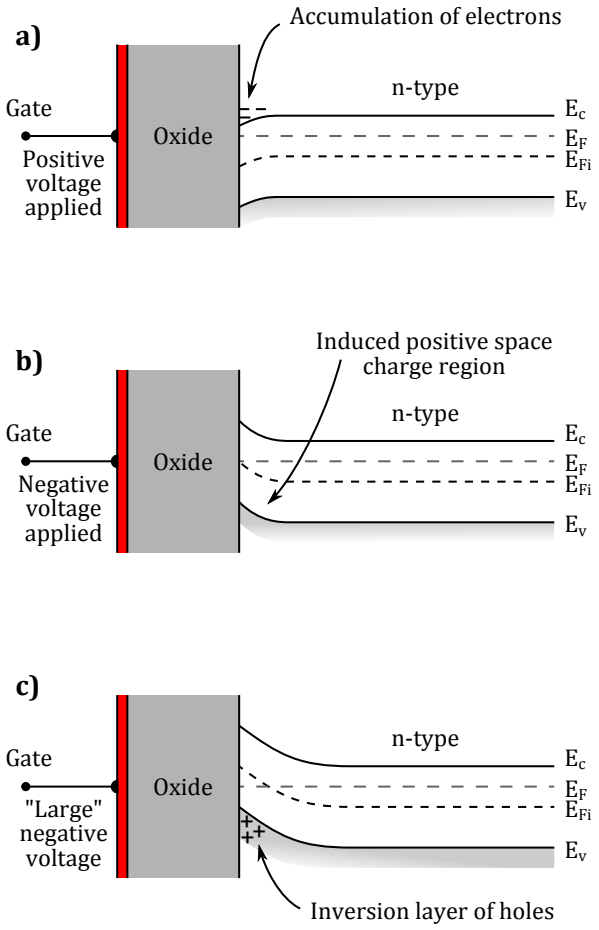

Figure 4.2: Energy-band diagram of an interface between an insulator and an inorganic *n*-type semiconductor for a) a positive gate potential, b) a moderate negative potential, and c) a "large" negative gate potential (from: [12])

erate negative potential, a *depletion* of majority charge carriers occurs in the *n*-type substrate. For a sufficiently large negative potential, the bands bend even further upward, and the intrinsic Fermi level crosses the Fermi level (4.2 c)). For this case the density of positive charge carriers, i. e. holes, exceeds that of electrons, and the *n*-type semiconductor close to the oxide interface becomes *p*-type. An *inversion* layer of holes has been created at the interface, which "connects" the highly doped *p*-type source and drain regions and turns the device on. One of the main advantages of the MOSFET structure lies in its highly doped contact areas: when no gate potential is applied, the contacts form p^+n junction diodes, one of which always acts as reverse-biased, ensuring very low off-currents [29].

Figure 4.1 b) shows an organic field-effect transistor. The source and drain electrodes form ohmic contacts directly to the conducting channel (i. e. the insulator-semiconductor interface). Unlike the MOSFET described above, the OFET works in the accumulation regime and not in the inversion regime. As the ohmic contacts exhibit no rectifying characteristics, low off currents are only guaranteed by the low conductivity of the semiconductor material. Figure 4.1 c) shows a three-dimensional sketch of the OFET structure, depicting the channel length L (i. e. the distance between source and drain contact) and the channel width W (which corresponds to the width of the metal contacts). To generate an easily interpreted graphic image the semiconductor layer was omitted. In the following, the device geometry and operating principles of a typical OFET are described in further detail.

4.2.1 OFET device geometry

There exist four widely used device geometries used for OFET applications, which are shown in Figure 4.3. As the field of organic transistors emerged from silicon technology, the *bottom-gate* structures are the most common ones used, where initially a single-crystal silicon wafer with a silicon-oxide layer on top worked as the substrate, gate contact and gate dielectric, respectively. Metal contacts for connecting the semiconductor are either applied directly on the dielectric (bottom-contact geometry) or on top of the semiconductor layer (top-contact).

The gate dielectric plays a key role for the electronic functionality of the transistor. Its capacitance (i. e. the thickness and permittivity) influences the number of charge carriers in the channel and therefore the operating voltage of the transistor, and its surface properties determine the molecular growth and orientation of the organic semiconductor which is deposited on top of it. Also, it must be robust enough to withstand all following fabrication steps, which may for example include chemical or thermal treatments.

To be applicable in low-cost and large-area production, the demands on the dielectric layer have changed over the past few years. A wide range of *organic* materials have been investi-

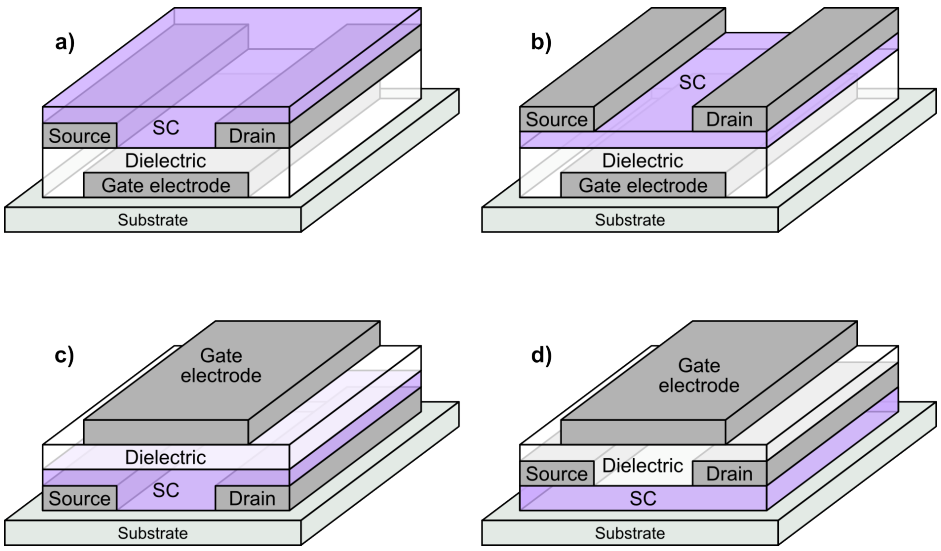

Figure 4.3: Schematics of 4 OFET geometries: a) bottom-gate bottom-contact, b) bottom-gate top-contact, c) top-gate bottom-contact, d) top-gate top-contact

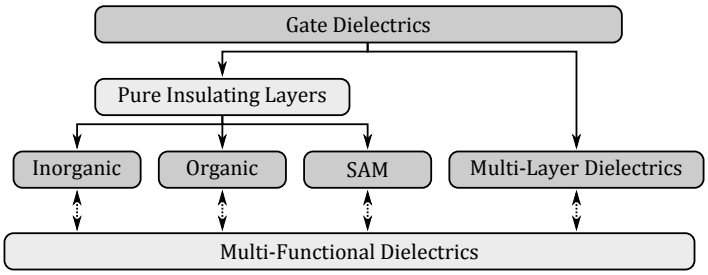

Figure 4.4: Schematic overview of gate dielectric materials used in OFETs (from: [31, chap. 6])

gated, including solution-processable polymer dielectrics [30], especially with respect to their ability to be used in flexible electronics on substrates like poly(ethylene terephthalate) (PET) foils [31, chap. 7] for roll-to-roll manufacturing. Another benefit of organic dielectrics is their application in top-gate transistor structures (Figure 4.3 c) and d), as an organic layer does not damage the semiconductor layer underneath, in contrast to inorganic dielectrics like sputtered aluminum oxide. Figure 4.4 shows a schematic representation of the different types of potential dielectrics, namely "pure" insulating layers like self-assembled monolayers (SAM) [32], inorganic and organic dielectrics, as well as their combinations used in multilayered structures. If more than just the insulating properties are of importance, a fifth group of multi-functional dielectrics arises, comprising for example of highly flexible [33] or transparent [34] dielectrics.

For the deposition of the organic semiconductor layer mainly two different methods are used. A simple and cost-effective way is *spin-coating* the conducting polymer from solution.

By adjusting the rotation speed, the film thickness can be well controlled, and smooth layers on large areas can be achieved. A prerequesit is the solubility of the polymer, which can be aided by attaching solubilizing groups to the polymer backbone. This is usually not possible for small molecules, therefore they are applied to the substrate by *vacuum evaporation*. For this technique the organic material is placed in a small quartz tube with the substrate a few centimeters above it. The evaporation chamber is then evacuated, and by heating the tube the material evaporates and condenses on the substrate. By monitoring the substrate temperature and the deposition rate the film thickness can be controlled. This method is not applicable for polymers, which tend to decompose at high temperatures [29].

4.3 Operating principle

The operating principle of organic field-effect transistors can be described by using a simplified energy-band diagram. Figure 4.5 a) shows the source and drain metal electrodes with the level of the Fermi energy, denoted by E_F, as well as the HOMO and LUMO of the organic semiconductor material. For an organic semiconductor without applied gate voltage, the Fermi level is somewhere in the bandgap, as the semiconductor material is intrinsically undoped, and aligned with the Fermi level of the metals. Due to the potential barrier between source and the energy levels of the semiconductor, injection of charge carriers is hindered. As there are also no intrinsic charge carriers in the material, no current can flow between source and drain electrode, and the transistor is in the off state.

If a positive gate potential is applied, electrons are accumulated at the semiconductor-dielectric interface ("interfacial doping"), and the Fermi level shifts towards the LUMO (Figure 4.5 b)). If the Fermi level of the source/drain metals is now close to the LUMO, electrons can be injected from the source into the semiconductor. By applying a positive potential to the drain electrode these charges can be extracted, and the transistor is switched on (4.5 c)). A semiconductor capable of conducting an electron current is termed *n-type*. As will be shown in the next section (Eq. (4.5)), the current is depending on both the gate voltage and the drain voltage. In order to increase the on current, the energetical barrier between the source/drain metal and the LUMO should be as small as possible. Therefore low work function metals are often chosen for contacting *n*-type transistors, such as calcium ($\Phi_{Ca} = 2.87$ eV), magnesium ($\Phi_{Mg} = 3.66$ eV) or samarium ($\Phi_{Sm} = 2.7$ eV) [35].

When applying a negative potential to the gate, holes are induced in the semiconductor adjacent to the gate dielectric, and the Fermi level shifts towards the HOMO (see Figure 4.5 d)). If a high work function metal is used for contacting the semiconductor, for instance gold with

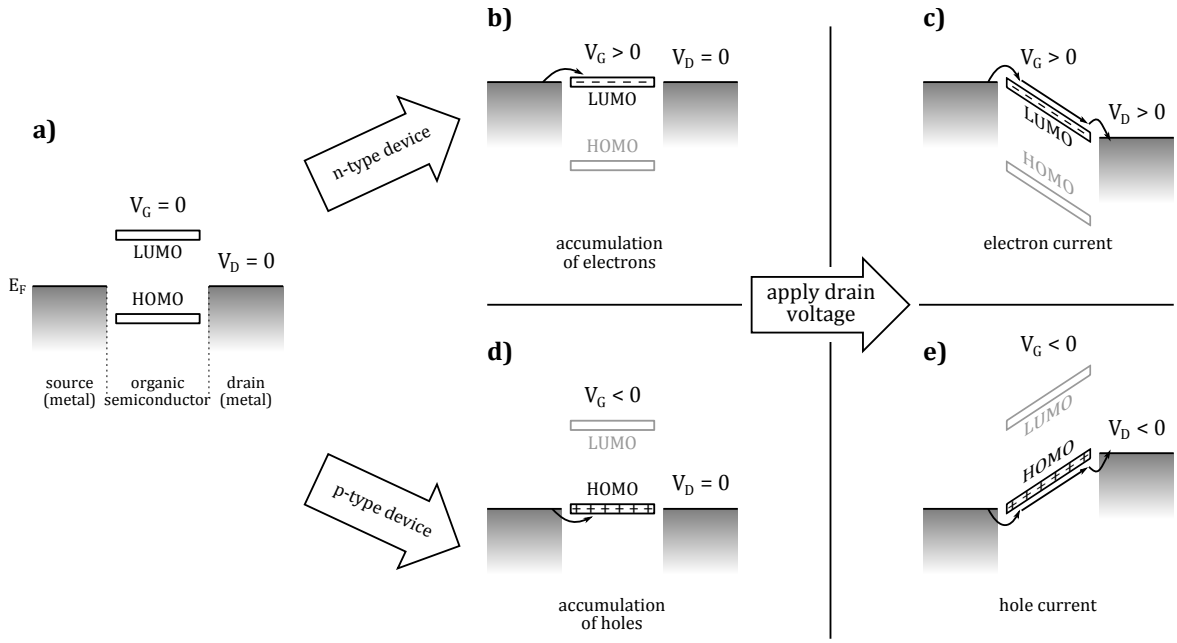

Figure 4.5: Simplified energy-band diagram of an organic field-effect transistor

$\Phi_{Au} = 5.1$ eV, the energy difference between the Fermi level and the HOMO is small, and holes can be injected. For a negative drain voltage ($V_D < 0$, see 4.5 e)) the charge carriers can be extracted and a hole-current is flowing between source and drain. A semiconductor which is conducting holes in this way is referred to as being *p-type*.

4.3.1 OFET current-voltage characteristics

In the following, the current-voltage (I-V) characteristics of an OFET are derived. Basically, an OFET can be seen as a parallel plate capacitor (see Figure 4.6), where one "plate" is a conducting channel expanding between two ohmic contacts, namely source and drain, and the other plate is formed by the gate electrode. The plates are seperated by the gate dielectric layer. The density of charge carriers n in the channel can be controlled by the applied potential to the gate.

If the drain electrode is at a potential V_D versus ground and the source electrode is connected to ground ($V_S = 0$), the induced field in the channel decreases linearly from drain to source, and the average potential in the channel is simply given by $V_{avg} = V_D/2$.

The total applied potential is then given as the average channel potential with respect to the gate potential V_G acting on the other side of the dielectric, $(V_G - V_{avg})$, and the number of

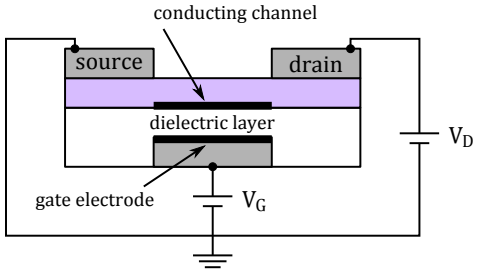

Figure 4.6: Schematic of an OFET acting as a parallel plate capacitor, controlled by the gate voltage V_G and the drain voltage V_D

charges Q on one capacitor plate, where C_i denotes the capacitance of the gate insulator and V the applied potential, is given by

$$Q = C_i \cdot V_{total} = C_i \cdot (V_G - V_{avg}) = C_i \cdot \left(V_G - \frac{V_D}{2}\right) \tag{4.1}$$

The current density in the channel is given by Ohm's law, which states that the current density equals the electrical conductivity times the electric field strength, $j = \sigma \cdot E$. The conductivity can be rewritten as a function of mobility μ,

$$\sigma = e \cdot n \cdot \mu \tag{4.2}$$

where e is the elementary charge and n the charge carrier density in the channel. The product of e and n equals the total number of charge carriers Q in the channel, which is exactly the charges accumulated at the "capacitor plate" given by Eq. (4.1).

$$\begin{aligned} j = \sigma \cdot E = e \cdot n \cdot \mu \cdot E = \\ = \quad Q \cdot \mu \cdot E = C_i \cdot \left(V_G - \frac{V_D}{2}\right) \cdot \mu \cdot E \end{aligned} \tag{4.3}$$

By using the relation between electric field strength and applied potential between two metal plates seperated by a distance L, $E = V_D/L$, defining the total drain current I_D between the source and the drain contact as the product of current density in the channel times the channel width, $I_D = j \cdot W$ (see Figure 4.7 for a schematic view), and substituting these relations into equation (4.3), a term for the drain current in dependence of gate and drain voltage is found:

$$I_D = \frac{W}{L} \cdot C_i \cdot \mu \cdot \left(V_G - \frac{V_D}{2}\right) \cdot V_D \tag{4.4}$$

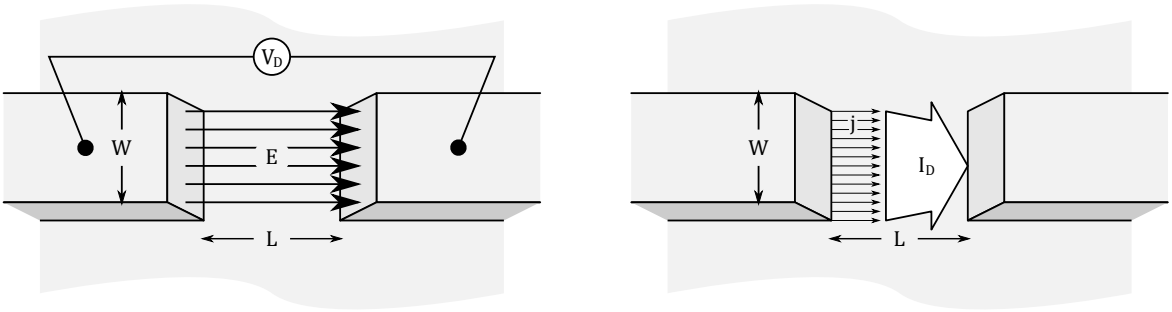

Figure 4.7: Illustration of the electric field and the drain current in a transistor channel

For this derivation, the *threshold voltage* V_T was assumed to be zero. The threshold voltage is the minimum gate voltage that is necessary to form the conducting channel. It takes into account various potential drops across the gate-insulator-semiconductor interfaces [31, chap. 1]. Therefore in a non-ideal device it can not be assumed to be zero, and the term of the gate voltage in Eq. (4.4) must be replaced by $(V_G - V_T)$:

$$I_D = \frac{W}{L} \cdot C_i \cdot \mu \cdot \left(V_G - V_T - \frac{V_D}{2} \right) \cdot V_D \tag{4.5}$$

This final derivation rests on two assumptions: (1) The transverse electric field in the channel which is induced by the gate voltage is much larger than the field along the channel, which is caused by the drain voltage. This is the so-called gradual channel (or Shockley) approximation, and it implies that the charge density in the channel is mainly related to a change in the gate voltage; (2) the mobility is constant all over the channel. Assumption (1) is justified by the device geometry, where the thickness of the dielectric (tens of nanometers) is usually much smaller than the channel length (tens of micrometer). Statement (2) however is not fulfilled in organic semiconductors, which leads to problems when trying to extract parameters from the current-voltage characteristics, as shown below.

4.3.2 Operating regimes

Important device parameters can be extracted from the current-voltage curve of an OFET, but Eq. (4.5) must first be analyzed in more detail to correctly describe the actual transistor behaviour.

As the drain current I_D is a function of two independent voltages, namely gate and drain voltage, it can be plotted in two different ways: if the gate voltage is used as the abscissa, the obtained plot shows the so called *transfer characteristics* of the transistor. A fixed value for

the drain voltage must be chosen for this characterisation; if the drain current for various gate voltage values is plotted as a function of drain voltage, the *output characteristics* of the device are shown. Figure 4.8 a) and c) show the transfer and output curves for a *p*-type OFET.

As the transfer characteristic is a function of gate voltage, it shows the difference between the off (zero gate voltage) and the on (larger gate voltage) state of the transistor. This so-called on/off ratio is schematically shown in Figure 4.8 b).

From the output characteristics three different operating domains can be distinguished, namely the linear regime, the pinch-off point and the saturation regime. They are depicted in Figure 4.8 d)–f), and described in the following.

For a small drain voltage, $V_D \ll V_G$, the charge carrier density in the channel is mainly dependent on the gate voltage and does not vary noticably from source to drain (Figure 4.9 a)). The term $\frac{V_D}{2}$ in Eq. (4.5) can be neglected in comparison to V_G, and the resulting current (for a fixed gate voltage) is linearly dependent on the drain voltage, as shown in Eq. (4.6). Therefore this is called the *linear regime*.

$$I_{D_{lin}} = \frac{W}{L} \cdot \mu \cdot C_i \cdot (V_G - V_T) \cdot V_D \tag{4.6}$$

If the drain voltage is increased to a value of $V_D \cong V_G - V_T$, the so-called *pinch-off* point is reached, and the electric potential at the drain contact becomes zero, as does the charge carrier density, which is now linearly decreasing from source to drain (Figure 4.9 b)).

Increasing the drain voltage beyong the pinch-off voltage does not further increase the drain current. The pinch-off point is shifted through the channel towards the source (Figure 4.9 c)), and the potential drop between this point of zero potential and the source electrode is at all times equal to the nominal field at the source, $V_G - V_T$. From this it is clear that for a higher gate voltage the saturation current must be higher and the pinch-off point must move to higher drain voltages. As the current is drain-voltage independent for $V_D \geqslant V_G - V_T$, the device is said to be operated in the *saturation regime*. It is described by Eq. (4.7), which immediatly follows from Eq. (4.5) by substituting V_D with $(V_G - V_T)$.

$$I_{D_{sat}} = \frac{W}{2 \cdot L} \cdot \mu \cdot C_i \cdot (V_G - V_T)^2 \tag{4.7}$$

As the drain current increases with the square of the gate voltage, the pinch-off points for different gate voltages must lie on a parabola, as shown in Figure 4.8 g).

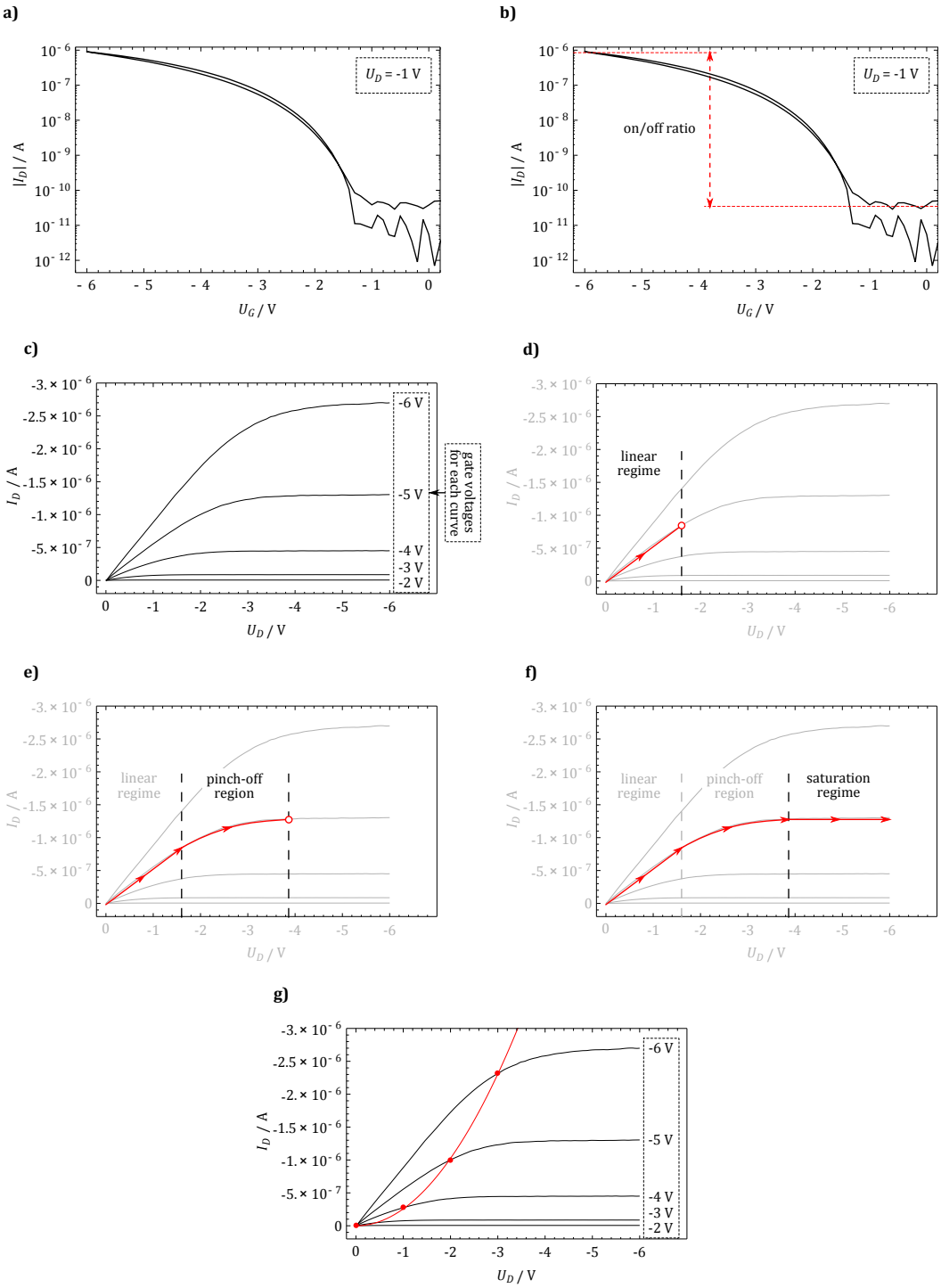

Figure 4.8: Typical a) transfer characteristics of an OFET, with the on/off ratio depicted in b); c) output characteristics of the same OFET, for gate voltages between -2 and $-6\,V$; d)–f) output curves illustrating the linear, pinch-off and saturation regime, respectively; g) output characteristics with the calculated values for the pinch-off points for each curve (red dots) and the fitted parabola (red line); Note that these curves were derived from a *p*-type OFET, therefore both the drain and the gate voltage are negativ, as is the drain current.

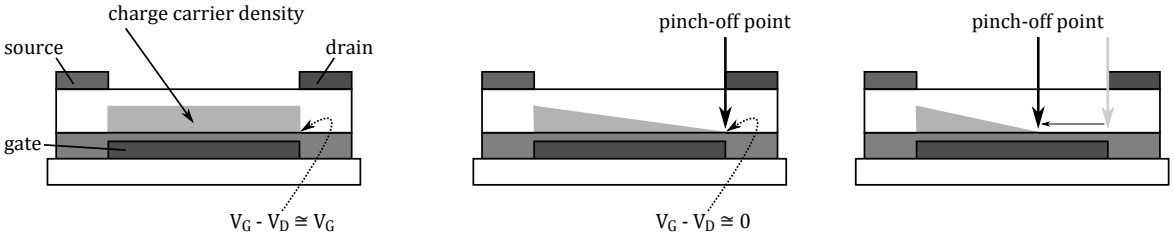

a) linear regime **b)** pinch-off point **c)** saturation regime

Figure 4.9: Variation of charge carrier density along the channel for different values of the drain voltage V_D. Note that the thickness of the channel represents the charge carrier density, and not its spacial extension

4.3.3 Parameter extraction

For modeling device operation for large circuits it is essential to precisely extract the necessary device parameters from the OFET current-voltage characteristics. In the following, methods for obtaining the charge carrier mobility, the threshold voltage and the contact resistance are presented.

Mobility As the drain current is directly proportional to the mobility μ, increasing the mobility is an important step for high performance OFETs. Measuring the mobility of a device is therefore most important.

There exist three main methods for determining the mobility. The probably most widespread technique consists of plotting the square root of the drain current in the saturation regime versus the gate voltage. According to Eq. (4.8) the outcome should resemble a straight line, with a slope proportional to $\sqrt{\mu}$.

$$\sqrt{I_{D_{sat}}} = \sqrt{\frac{W \cdot C_i}{2 \cdot L}} \cdot \sqrt{\mu} \cdot (V_G - V_T) \tag{4.8}$$

However it is important to note that Eq. (4.7) was derived under the assumption of constant mobility. This is usually not the case in organic semiconductors, where the mobility shows a gate-voltage dependence [29, 36]. This especially poses a problem for this extraction method, as the deviation of the expected straight line from the actual experimental data at low gate voltages can be either due to a lower mobility or because of entering the sub-threshold voltage regime. Furthermore, as described earlier, the charge carrier density in the channel is not uniform in the saturation regime. Depending on the gate and drain voltage values, the pinch-off point is somewhere in the middle of the conducting channel, and the assumption of a constant mobility in the accumulation as well as in the depletion zone cannot hold.

Another approach for parameter extraction uses the first derivation of the linear-regime drain current versus the gate voltage, the so-called transconductance g_m (Eq. (4.9)), thus avoiding the problem of pinch-off and without assuming a constant mobility.

$$g_m = \left| \frac{\partial I_D}{\partial V_G} \right|_{V_D=const} = \frac{W}{L} \cdot \mu \cdot C_i \cdot V_D \tag{4.9}$$

However, if the mobility is gate-voltage dependent, the exact expression for the first derivative is

$$g_m = \left| \frac{\partial I_D}{\partial V_G} \right|_{V_D=const} = \frac{W}{L} \cdot C_i \cdot V_D \cdot \left(\mu + (V_G - V_T) \frac{\partial \mu}{\partial V_G} \right), \tag{4.10}$$

so that the method is only valid when the second term, expressing the variation of mobility with respect to gate voltage, can be neglected.

A third method to determine the mobility is the transfer line method (TLM), which is described in further detail in the following section concerning the *contact resistance*.

Threshold voltage As mentioned earlier the threshold voltage V_T is the minimum gate voltage that is necessary to form the conducting channel. It is a crucial device parameter for circuit modeling, as all transistors in a circuit should switch on at the same voltage. There exist numerous techniques for extracting the threshold voltage from the transistor characteristics, most of them originating from the field of conventional silicon MOSFETs. As shown by Boudinet et al. [37], most of this techniques are not applicable for OFET characterisation, or yield doubtful results for small channel lengths. The authors therefore recommend the use of either the ratio method (RM) or the second derivative (SD) method. Also the ELR method (extrapolation in the linear region) is shortly described, as it gives a very demonstrative approach to determine the threshold voltage from a transfer curve.

For the *ratio method*, the drain voltage divided by the square root of the transconductance is plotted versus the gate voltage, yielding a linear function for higher values of V_G. The intersection of the gate-voltage axis with a linear extrapolation of this data yields the threshold voltage. One drawback of this method is that the voltage range over which the extrapolation should be operated is not clearly defined.

The *second derivative method*, which was developed by Wong and coworkers [38] under the name of "transconductance change method", uses the second derivative of the drain current with respect to the gate voltage (which is exactly the change, or first derivation, of the transconductance, $\frac{d^2 I_D}{dV_G^2} = \frac{dg_m}{dV_G}$), which is supposed to have a peak maximum denoting the threshold voltage. This can be justified by the following model, which is depicted in Figure 4.10: Assuming that the drain current is zero for $V_G < V_T$ and rises linear with the gate voltage for $V_G > V_T$, the

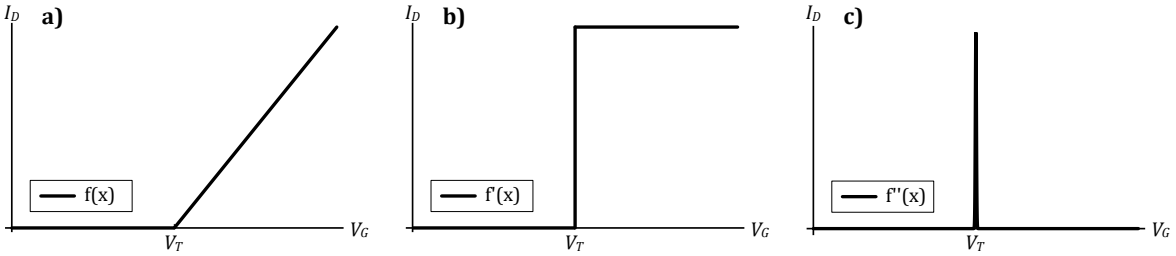

Figure 4.10: Model for the SD method: a) simplified drain current I_D, being zero for $V_G < V_T$ and rising linear for $V_G > V_T$; b) first derivation of I_D with respect to V_G; b) second derivation of I_D

first derivation of I_D (i. e. the transconductance) has the form of a step function, and the second derivation the form of a Dirac delta function (approximated in c) by a narrow Gaussian function). In practice, the drain current does not have a sharp kink at the threshold voltage, but a somewhat blurred transition from off to on state. Therefore the second derivation resembles more the shape of a Gaussian than that of a delta function, with its maximum indicating the threshold voltage.

When using the *ELR method*, the transfer curve is linearly extrapolated from the point of its maximum first derivative, the line representing a tangent to the linear region of the transfer curve. The threshold voltage is then calculated as the intersection of this line with the gate voltage axis at $I_D = 0$ plus $V_D/2$. An application of this method as well as the SD method is shown later on in Chap. 8, Figure 8.2 and 8.3.

Contact resistance When discussing the total resistance R_{on} between source and drain while an OFET is switched on, the transistor can be thought of as three resistors connected in series, as depicted in Figure 4.11, namely the contact resistance R_c between the semiconductor and the source and drain metal electrodes plus the channel resistance R_{ch}.

$$R_{on} = (R_{source-SC} + R_{drain-SC}) + R_{channel} = R_c + R_{ch}$$

These resistances pose a limiting factor to the device performance, as they directly control the drain current. It is therefore of importance to know these values and keep them as low as possible. Measures known from the literature to achieve low contact resistances include the deposition of self assembled monolayers [39], UV/ozone treatment of the source and drain contacts [40] or chemical doping of the semiconductor [4].

One possibility to measure the contact resistance of a device is by using the *transfer line method* (TLM) [37, 41]. Other methods, including four-point measurements [42] or Kelvin probe force microscopy [43], are also possible but are not explained here. For obtaining the

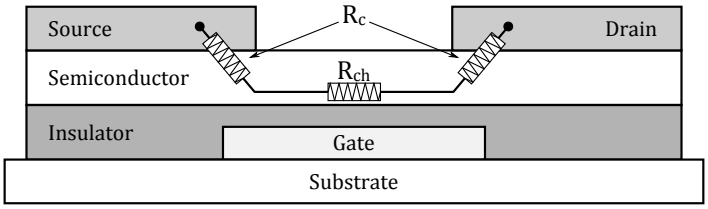

Figure 4.11: Sketch of a bottom-gate top-contact OFET, depicting the contact resistances R_c and channel resistance R_{ch}

working principle of the TLM, an ohmic potential drop is introduced in the equation for the drain current in the linear regime (Eq. (4.6)). This is done by replacing V_D by $(V_D - R_c \cdot I_D)$, and by rewriting the equation one obtains

$$R_{on} = \frac{V_D}{I_D} = \frac{L}{W \cdot \mu \cdot C_i \cdot (V_G - V_T)} + R_c \,. \tag{4.11}$$

Muliplying both sides of the equation by the channel width, a formula for the so-called width-normalized total resistance is obtained.

$$R_{on} \cdot W = \frac{L}{\mu \cdot C_i \cdot (V_G - V_T)} + R_c \cdot W \tag{4.12}$$

The total resistance equals the sum of the channel resistance, which is directly proportional to the channel length L in the linear regime, and the contact resistance which is assumed to be constant.

To obtain the contact resistance, the transfer curve in the linear regime must be measured for several OFETs with different channel lengths. Then the width-normalized resistance is calculated as a function of $(V_G - V_T)$ and plotted for all devices in a graph versus the channel length [37, 44]. Linear extrapolation of the data points for one fixed value of $V_G - V_T$ to zero channel length yields the contact resistance $R_c \cdot W$, as exemplified in Figure 4.12.

$$R_{on} \cdot W = \left.\frac{V_{D_{lin}}}{I_D}\right|_{V_D \ll V_G} \cdot W = \frac{L}{\mu \cdot C_i \cdot (V_G - V_T)} + R_c \cdot W \quad \xrightarrow{L \to 0} \quad R_c \cdot W \tag{4.13}$$

Furthermore the gate-voltage dependent mobility can be extracted from the slope of the line. This method is very sensitiv to the value of the threshold voltage, which makes it important to carefully determine V_T in the linear regime.

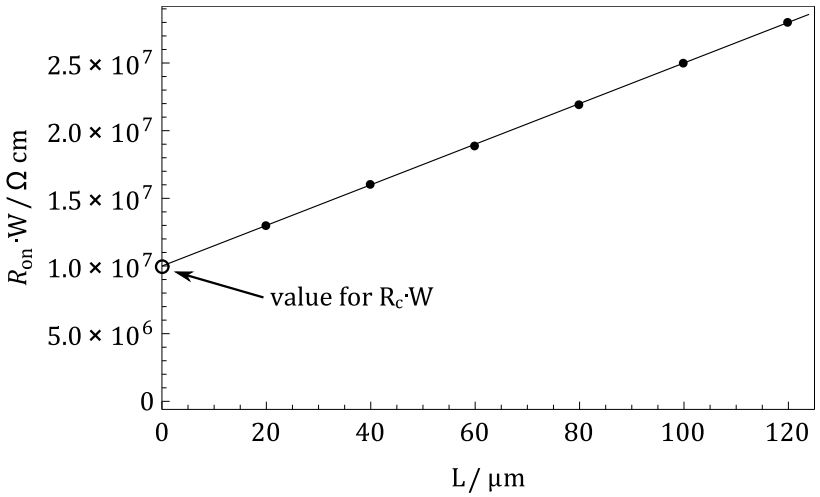

Figure 4.12: Virtual example for the TLM, showing the total resistance values of six devices with varying channel length between 20 and 120 micron and the linear extrapolation for the contact resistance $R_c \cdot W$

Part II

Experimental

5 OFET device preparation

As stated earlier (Sec. 4.2.1) there exist four different device geometries used for OFETs. All experiments described in the following chapters were performed with bottom-gate top-contact transistors. The device preparation process will be described in the following, an illustration of the final sample is shown in Figure 5.9.

5.1 Substrate and gate electrode preparation

Glass plates of the size of 15 mm × 15 mm serve as the device substrate. They are thermally and chemically stable and can endure all further processing steps. Every glass plate ("sample") is first cleaned in a 3 : 1 mixture of ammonia[aq] (NH_4OH) and hydrogen peroxide[aq] (H_2O_2) in water ("base piranha etch"), immersed in an ultrasonic bath at 80 °C to rid the substrate of organic residues.

As a first production step aluminum is deposited on the substrate, to serve as a gate electrode. This was performed by vacuum evaporation of the metal, where a shadow mask was used to define the structure (for details see 5.5). A sketch of the shadow mask is shown in Figure 5.8, with the lateral dimensions of the gate electrode being 1 mm × 10.5 mm and a typical aluminum thickness of 150 nm.

5.2 Al_2O_3 as a gate dielectric

For the gate insulator, aluminum oxide (Al_2O_3) was electrochemically grown on the aluminum surface by galvanostatic anodization in 0.01 mol l^{-1} citric acid. The glass substrate with the applied aluminum layer was immersed in the electrolyte solution, together with a platinum counter electrode (see Figure 5.1). The electrolyte solution was stirred and degassed with nitrogen gas during the whole anodization process. As described in further detail in appendix A, a constant current density of 0.6 mA cm^{-2} was applied, and by using equation (A.5), which shows a direct relation between anodization time t and oxide thickness d, Al_2O_3 layers with

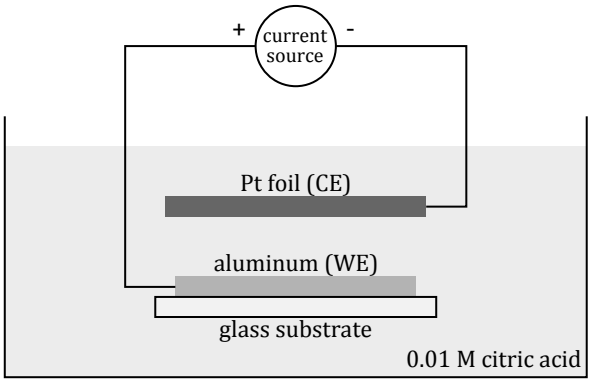

Figure 5.1: Sketch of the anodization setup, with the aluminum deposited on a glass substrate as a working and a platinum foil as a counter electrode

thicknesses between 16 and 80 nm could be obtained, corresponding to anodization times between 1 and 5 minutes respectively.

Following the anodization the sample is kept in an ultrasonic bath of deionized water at 80 °C for several minutes, where the oxide swells up due to water uptake and pinholes are closing. Afterwards the sample is heated up to 200 °C in an oven under reduced pressure for several hours to get rid of all water residues.

This galvanostatic anodization process is in contrast to other methods found in the literature, where the anodization is performed by "ramping up the voltage up to a limiting anodisation voltage V_A", and the final thickness of the film is determined by the "anodisation ratio" $c_{Al} \approx 1.3\,\mathrm{nm/V}$ [45–47].

From the process of anodization it is clear that this method is only applicable for bottom-gate structures. Anodizing a top-gate device, be it that the semiconductor does not degrade in the electrolyte, would only yield an oxide *on top* of the aluminum, but not on the semiconductor-aluminum *interface* where it is needed.

Using aluminum oxide as a gate dielectric provides several advantages. Aluminum is a cheap starting material, and can be applied to any substrate by evaporation techniques as well as by sputtering. Aluminum oxide is pinhole-free, has very low leakage currents and high breakdown field strengths [46]. The leakage curve for a typical OFET is shown in Figure 8.1, whereas Figure 5.2 shows a measurement of the breakdown voltage for a sample with a 16 nm thick oxide. As can be seen significant leakage starts above a value of about $4.5\,\mathrm{MV\,cm^{-1}}$. The sample was prepared as a metal-insulator-metal (MIM) structure, where the Al_2O_3 layer was sandwiched between two Al electrodes.

Another advantage of Al_2O_3 is its high dielectric constant of $\varepsilon_r \cong 9.34$ [48]. This, combined with the fact that a thin oxide of thickness $d = 16\,\mathrm{nm}$ already yields a dense film, provides

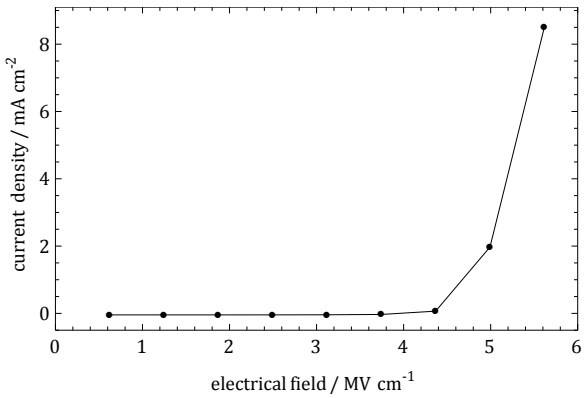

Figure 5.2: Measurement of the leakage current of 16 nm Al_2O_3 sandwiched between two Al electrodes

a high capacitance ($C \sim \varepsilon_r/d$) which directly influences the number of charge carriers in the channel and therefore the drain current in the OFET (Eq. (4.1) and (4.5)). An oxide film of $d = 16$ nm for example would yield a capacitance of 517 nF cm^{-2}.

5.3 Influence of interfacial layers

Although Al_2O_3 seems to be a very promising dielectric in terms of electronic propierties, its surface properties seem to decline the current characteristics of the OFET. It has been shown that for devices using C_{60} as a semiconducting material, the introduction of an interfacial layer between Al_2O_3 and semiconductor improves the threshold voltage as well as the overal transistor performance [49]. Other works show that by introducing a self-assembled monolayer at the Al_2O_3 surface, the mobility of pentacene transistors for low gate voltages can be enhanced [50].

For this work pentacene was used as the semiconducting material (see next section for details), and different interfacial layers were tested for their influence on the device performance (see Figure 5.3 for the chemical structures). Polyvinyl alcohol (PVA) is known to perform well in pentacene transistors [1], therefore it was used for the first few devices. To obtain hysteresis free transistors,"dialysis-grade" PVA was used [51], diluted in deionized water to a 100 parts per million solution. The 100 ppm PVA solution was then spun onto the aluminum oxide at 1500 revolutions per minute (rpm). However, PVA is dissolved in water, and by spin coating not all water residues may leave the PVA film. Several groups have studied the influence of water being absorbed by the bulk of the organic semiconductor film, which may lead to an increase of the off-state conduction, a trapping of charge carriers and a lack of saturation in the output characteristics [31, chap. 5]. For these reasons another interlayer was tested.

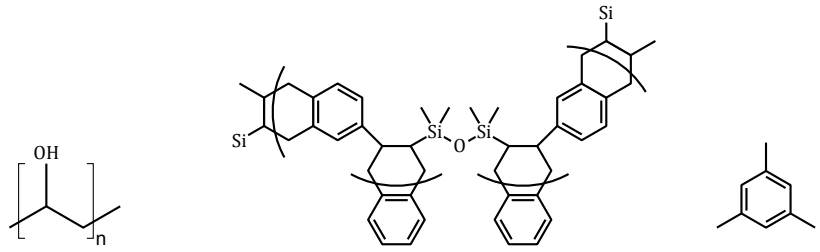

Figure 5.3: Chemical structures of PVA and BCB, used as interfacial layer in pentacene OFETs, as well as mesitylene, the solvent of BCB

Divinyltetramethyldisiloxane-bis(benzo-cyclobutene) (BCB) is often used in OFETs, especially in combination with *n*-type materials [49, 52, 53], and it is dissolved in mesitylene (C_9H_{12}), avoiding the problem of water residues in the system. A precursor solution of 0.1 wt$\%$ BCB (Cyclotene™ 3022-35, Dow Chemicals) in mesitylene (Acros Organics, 97 $\%$) was spun at 1500 rpm onto the Al_2O_3 film, yielding a thickness of around 6 nm. The samples were then annealed at 180 °C for cross-linking.

The thickness of the dielectric layers was measured by using a MIM device with two seperate top contacts (see Figure 5.4). The first capacitance measurement was performed directly on top of the Al_2O_3 layer (contact $M1$), yielding capacitance $C1$. The second capacitance value was measured on contact $M2$, which is on top of both Al_2O_3 and BCB, yielding capacitance $C2$. The difference in capacitance values relates to the thickness d of the BCB layer (with the area A being known and $\varepsilon_{r(BCB)} = 2.65$ according to [54]) as

$$d = \frac{\varepsilon_0 \cdot \varepsilon_{r(BCB)} \cdot A}{\left(\frac{C1 \cdot C2}{C1 - C2}\right)} \quad .$$

OFETs using pentacene on an 80 nm aluminum oxide with different interfacial layers were prepared in the same production process. The resulting transfer curves are shown in Fig-

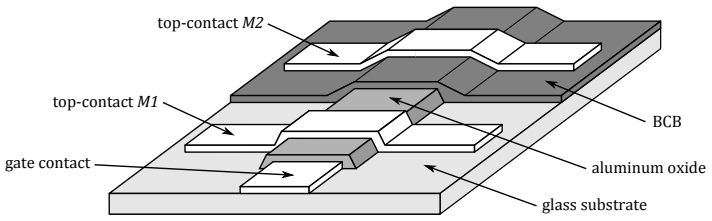

Figure 5.4: Illustration of a metal-insulator-metal (MIM) device with 2 top-contacts

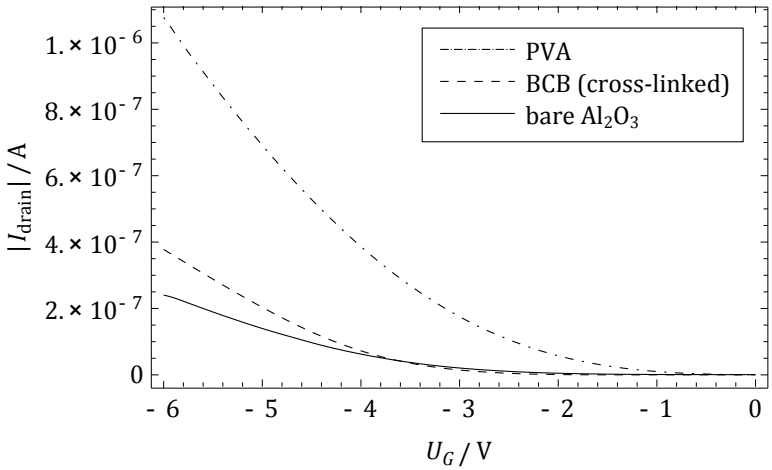

Figure 5.5: Transfer characteristics of a pentacene OFET at $V_D = -2$ V using aluminum oxide as a dielectric layer and PVA and cross-linked BCB as additional interfacial layers

ure 5.5. The threshold voltages for the three devices are very similar, ranging from -3.9 V to -4.0 V. As can be seen the device with BCB on top of the aluminum oxide displays a higher drain current than the sample with bare aluminum oxide. The sample with PVA on top of the Al_2O_3 however is performing even better, with the current at $V_G = -6$ V almost a factor of 3 higher than the one for BCB.

5.4 Pentacene as organic semiconductor

Pentacene, which was used as the semiconducting material for all devices in this work, is a *p*-type small molecule from the group of linearly fused benzene rings, or *oligoacenes* [55]. The chemical structures of the oligoacene repeating unit and pentacene are shown in Figure 5.6. Pentacene is widely studied since the 1970s (see for example [56]), and has shown mobilities of up to 3 $cm^2\ V^{-1}\ s^{-1}$ in devices using polymer gate dielectrics [57]. Recently, a group from IBM was able to image a single pentacene molecule with atomic resolution using an atomic force microscope (AFM) [58]. The picture can be seen in Figure 5.6.

Pentacene was evaporated in high vacuum ($p \sim 10^{-6}$ mbar) in a UNIVEX350 evaporation system (Leybold) with a growth rate of 0.4 Å s^{-1} to a film thickness of usually 50 nm in OFET devices. For pentacene samples used in spectroscopic and electrochemical measurements larger thicknesses of 100 to 200 nm were used.

To avoid degradation of the pentacene due to moisture and oxygen, the samples were immediately put into inert nitrogen atmosphere inside a glovebox after evaporation.

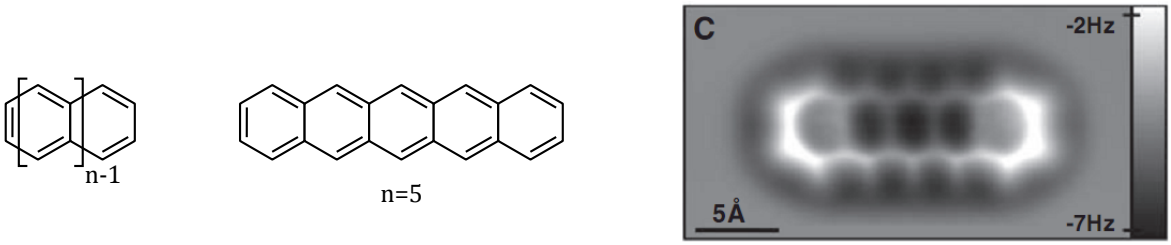

Figure 5.6: Chemical structures of the repeating unit of oligoacenes (left) and a pentacene molecule (middle); AFM image of a single pentacene molecule (right, from: [58])

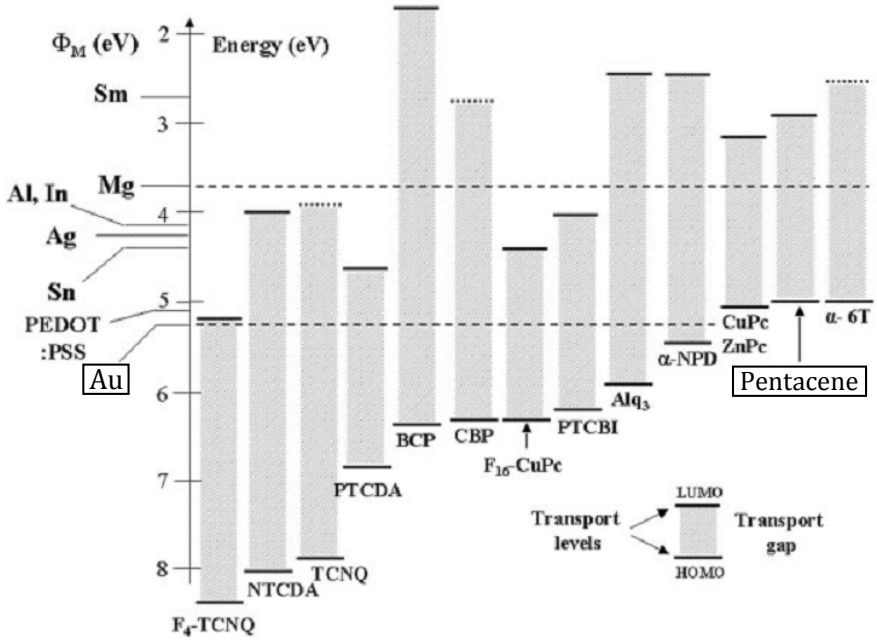

Figure 5.7: Comparison of metal work functions Φ_M on the left and ionisation energies and electron affinities, or HOMO and LUMO positions respectively, on the right. (from: [59])

5.5 Top contacts and final sample structures

As a final step in the transistor preparation process the top metal contacts were applied. As shown in Figure 5.7 the ionisation energy of pentacene ($IE = 5.0$ eV), i. e. the HOMO level, is sligthly smaller than the workfunction of gold (Au, $\Phi_{Au} = 5.2$ eV), leading to a good hole injection contact [59].

The Au contacts were deposited the same way as the aluminum gate metal in a high vacuum evaporation chamber, with the applied current and deposition rate controlled by a AS053 (Leybold) and a IL820 (Intellemetrics) controller, respectively. The metal is put into a tungsten

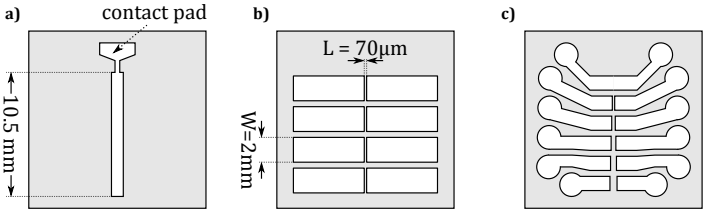

Figure 5.8: Pattern of the shadow masks used for metal evaporation: a) mask for the gate contact; b) standard transistor mask; c) transistor mask with varying channel length for TLM measurement

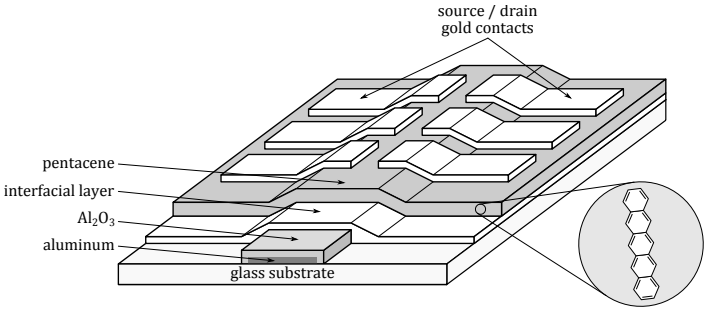

Figure 5.9: Three-dimensional illustration of the final OFET sample, showing from top to bottom: glass substrate, aluminum gate contact, Al_2O_3 gate dielectric, interfacial layer, semiconductor and three of the four source-drain pairs

boat, with the samples positioned a few centimeters above it, and the system is evacuated to a pressure of $p \sim 10^{-6}$ mbar. By heating the boat the material inside evaporates and deposits on the sample. The structures are defined by a steel foil shadow mask positioned right under the sample. The evaporation chamber is positioned inside a glovebox with slight nitrogen overpressure, avoiding contamination with oxygen and moisture. Therefore the samples can be put in and out of the evaporation system without the danger of degradation due to contact with ambient air.

Different shadow masks were used for different device architectures, as shown in Figure 5.8. For conventional field-effect transistors, four source-drain pairs (i. e. four "devices") were applied onto one sample, with channel dimensions of $W = 2$ mm and $L = 70$ µm. A three-dimensional sketch of the final sample is shown in Figure 5.9. For measuring the contact resistance with the transfer line method (TLM), devices with varying channel length were necessary. Therefore a new mask was designed to apply six devices onto one sample. The channel width was constant at $W = 1$ mm, whereas the channel length was varied in steps of 20 µm from 20 to 120 µm. Unfortunately the steel foils used as masks could not support a structure as small as 20 µm. The small bar seperating the first source-drain pair broke off, and therefore the first contact on every sample was shorted and could not be used for any measurement.

6 Electrochemistry and spectroscopy

6.1 Experimental setup

For the electrochemical and spectroelectrochemical experiments an electrolyte solution of 0.1 M tetrabutylammonium hexafluorophosphate ($TBAPF_6$, Fluka, 99 %) dissolved in acetonitrile (ACN, Merck, 99.9 %) was used. As ACN is hygroscopic, all electrochemical experiments were conducted in inert nitrogen atmosphere inside a glovebox, as water in the elctrolyte solution would influence the redox reaction of pentacene. Furthermore pentacene itself is not completely air-stable and would degrade due to oxygen and moisture in ambient air. For the *in-situ* IR and UV-VIS measurements, which were conducted outside of the glovebox, the pentacene sample was positioned inside a sealed compartment.

The electrodes in the electrochemical setup consisted of a platinum counter electrode (CE), an AgCl coated silver wire (Ag/AgCl electrode) as a quasi-reference electrode (QRE) and different types of working electrodes (WE), depending on the necessities of the experiment. The reference electrode was calibrated versus the ferrocene/ferrocenium couple before every measurement, with a redox potential of 350 mV. All the potential data reported in this work are, if not differently stated, measured against this reference electrode. A schematic representation of the setup is shown in Figure 6.1.

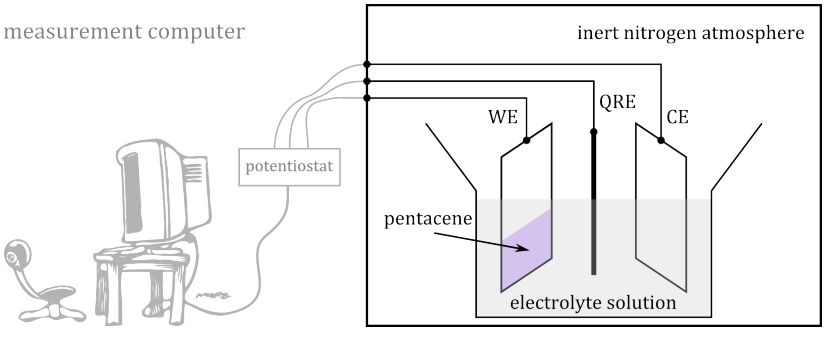

Figure 6.1: Sketch of the electrochemical setup in inert atmosphere

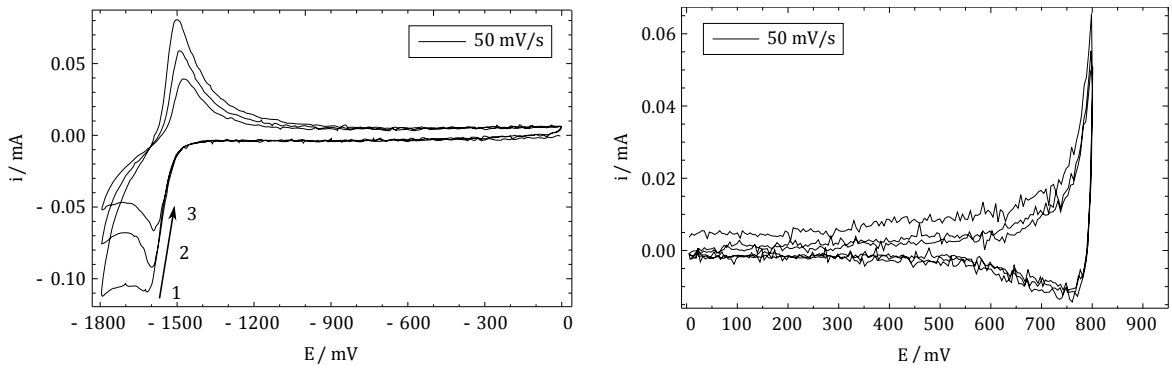

Figure 6.2: Cyclic voltammograms of pentacene evaporated on Pt foil, recorded for reduction (left) and oxidation (right), using a 0.1 M $TBAPF_6$-ACN electrolyte solution. Numbers 1–3 refer to the first, second and third cycle respectively

6.2 Electrochemical measurements

To gain an idea of the material properties of pentacene, cyclic voltammetry (CV) and electrochemical voltage spectroscopy (EVS) were conducted. Films of pentacene with a thickness of 200 nm were deposited on Pt foils by vacuum evaporation to serve as working electrodes.

At first, the reduction (corresponding to electrochemical *n*-doping) of pentacene was investigated. The potential E between working and counter electrode was swept from zero to -1800 mV and back to zero for three full cycles, with a scan rate of 50 mV s^{-1}. As shown in Figure 6.2 (left) a symmetrical redox response with well-defined reduction and reoxidation peaks at -1.6 and -1.5 V respectively can be observed in the cyclic voltammogram. However, a slight decrease in the redox response of the material can be seen upon continuous cycling. This can be explained in terms of the high solubility of the reduced pentacene in the electrolyte solution.

The *p*-doping was studied by oxidation of the pentacene, with the potential being swept between 0 and 800 mV and back to zero for three full cycles. From Figure 6.2 (right), it can be seen that the material does not give any well-defined oxidation peaks but rather an increasing oxidation current. On the reverse scan, a broad cathodic peak can be seen at approximately 0.7 V. When the pentacene film was cycled to higher switching potentials of 0.9 V (Figure 6.3) a decrease in the current response can be observed which can be ascribed to some degradation processes occurring at this potential. Thus, based on these experimental results, it can be concluded that the pentacene exhibits its best p-doping process at 800 mV.

To get an overview of the whole redox process, a full CV measurement for both the *p*- and the *n*-side was recorded, with the potential being swept from zero to 800 mV, down to -1800 mV and then back to zero again, with a scan rate of 10 mV s^{-1}. The resulting redox response can

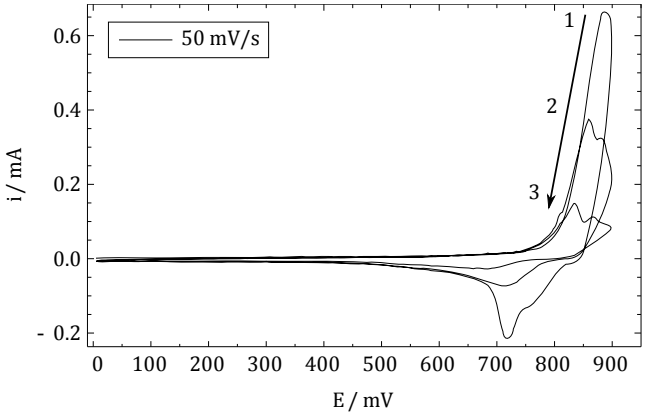

Figure 6.3: Cyclic voltammogram showing the degradation of pentacene for a switching potential of 0.9 V. Numbers 1–3 refer to the first, second and third cycle respectively

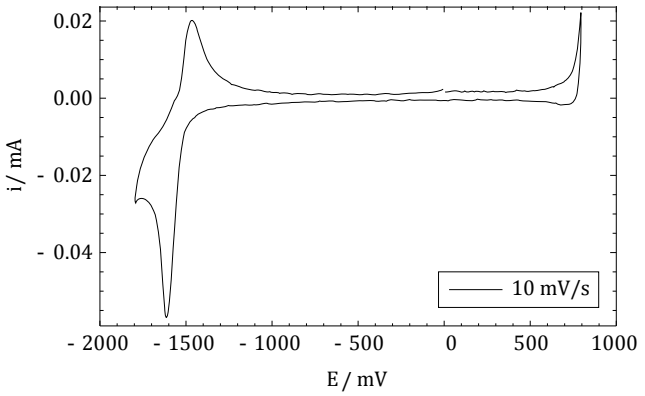

Figure 6.4: Cyclic voltammogram of pentacene evaporated on Pt foil, using a 0.1 M $TBAPF_6$-ACN electrolyte solution

be seen in Figure 6.4. The measurement signals an oxidation peak at around 800 mV and a reduction peak at around −1600 mV.

To exactly determine the onset of oxidation and reduction *electrochemical voltage spectroscopy* (EVS) measurements were conducted. The EVS method, developed by Thompson [60], consists of a series of constant potential steps, slowly ramping up to the maximum set potential. At each step the system is given a certain time interval to reach an equilibrium position, and the current decays. By integrating the current per time a value for the change in charge ΔQ in the system is obtained. Plotting the charge change in each potential step versus the potential ($\Delta Q/\Delta E$ vs E), the onset of oxidation or reduction can be determined very precisely. From the EVS data for pentacene an onset of the oxidation at 720 mV and onset of reduction at −1470 mV were obtained, summing up to an electrochemical bandgap of around

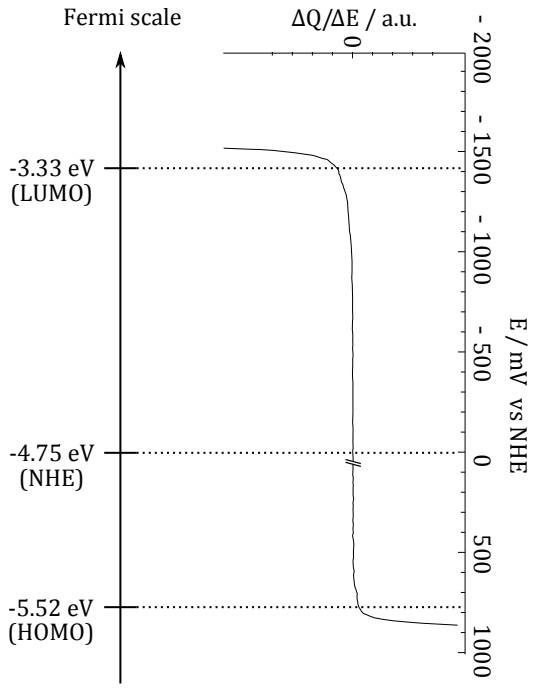

Figure 6.5: Energy levels of the HOMO and LUMO with respect to the NHE (left), corresponding to the EVS measurements for oxidation and reduction (right)

$E_g^{EC} = 2.2$ eV, which is in good agreement with values found in the literature [61, and references therein].

Despite the bandgap, also the energetic levels of the pentacene are important since they have to fit into the energy scheme of a transistor. The onset values for oxidation and reduction obtained from the EVS measurements were used to estimate the HOMO and LUMO levels of pentacene.

As the potential value of the QRE was determined as 50 mV versus NHE by calibration with a ferrocene couple, the onset values for oxidation and reduction are 770 and -1420 mV after correction, and can then be related to the Fermi scale which states the energy levels in electron volt. Figure 6.5 shows the edges for the HOMO and LUMO levels versus NHE in the Fermi scale, as well as the EVS measurements for oxidation and reduction, put together into one graph. The value of the NHE was chosen as -4.75 eV [62].

To further investigate the behaviour of pentacene during the processes of oxidation (*p*-doping) and reduction (*n*-doping), changes in the spectroscopic properties of the material were monitored as the redox reactions proceed by *in-situ* UV-visible (UV-VIS) and FTIR-attenuated total reflection spectroscopy (FTIR-ATR).

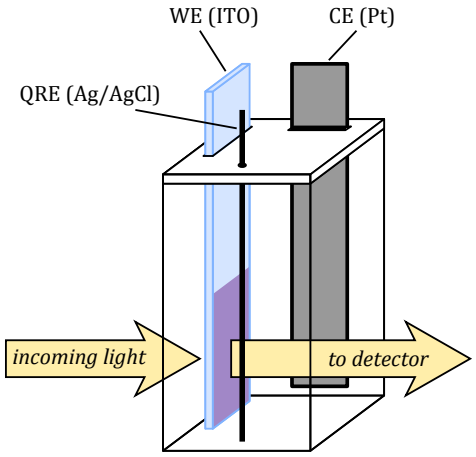

Figure 6.6: Illustration of the sealed cuvette used for UV-VIS measurements

6.3 UV-visible spectroscopy

For the UV-VIS measurements pentacene was evaporated on a stripe of indium tin oxide covered glass (ITO) acting as the working electrode. The sample was then put into a sealed cuvette, together with a platinum (Pt) counter electrode and a Ag/AgCl quasi-reference electrode. An illustration of the cuvette is shown in Figure 6.6. The metal electrodes are placed in such a way that they do not interfere with the optical path, and the light can pass through the cuvette and the material on the ITO electrode and reach the detector.

The wavelength of the light was scanned from 350 to 850 nm, using a Varian 3G UV-VIS spectrophotometer. The background spectra were always recorded with two blank ITO glasses. The cell was connected to a computerized electrochemical system and a potentiostat (Jaissle 1030 PC.T). As it takes several minutes for one scan of the wavelength, the electrochemistry could not be done in one full cycle but at different constant potentials.

The absorption spectra of pentacene in the UV-VIS during *p*- and *n*-doping are shown in Figure 6.7. In the neutral form four absorption peaks are visible, with the maximum at around 670 nm corresponding to the $\pi - \pi^*$ transition in pentacene. The local maxima at around 540 and 580 nm are due to higher vibronic transitions [63].

Upon oxidation changes can be observed in the material, mainly the appearance of a new feature around 420 nm and the decrease in absorption between 500 and 700 nm. The presence of an isosbestic point, seen at 590 nm, evidences the transition of the pentacene from one state to another.

In the *n*-side changes are less pronounced, with the most distinctive feature being an increase in the absorption below 500 nm at higher negative potentials.

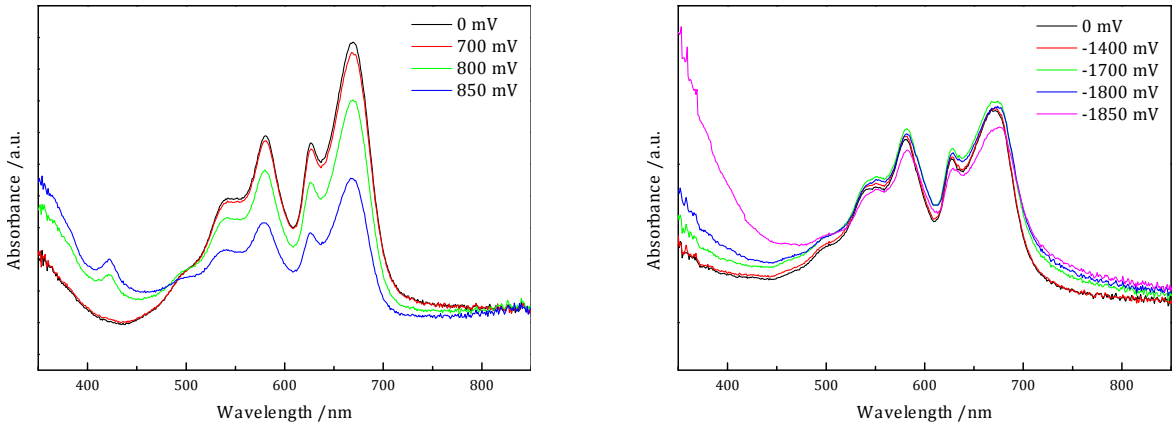

Figure 6.7: UV-VIS absorption spectra of pentacene during *p*- (left) and *n*-doping (right) at different potentials in 0.1 M $TBAPF_6$-ACN solution

From these different material behaviours upon *p*- and *n*-doping it is clear that the nature of the different charge carriers (electrons and holes) is very different in pentacene. This is also observed in the infrared regime, as shown in the following.

6.4 Infrared spectroscopy

The infrared spectra were recorded with a FTIR spectrometer (Bruker IFS66S) using a Mercury Cadmium Telluride (MCT) detector cooled with liquid nitrogen prior to the measurements. The experimental setup for the *in-situ* FTIR-ATR method consists of a small-size ATR spectroelectrochemical cell made from Teflon, as it is schematically shown in Figure 6.8. 200 nm of pentacene were evaporated on a germanium (Ge) reflection element, which served as the working electrode, and seals the Teflon cell on one side. Before mounting, the Ge element was polished with diamond paste (1 and 0.25 µm) and rinsed in a reflux system with acetone for 30 min. Adjacent to the Ge crystal the Pt working electrode and the Ag/AgCl quasi-reference electrode are placed, and the whole cell is sealed with paraffin wax. To avoid the accumulation of charged species formed in the electrochemical cell, the electrochemical cell was permanently purged with fresh electrolyte solution.

The redox response of pentacene was studied by recording the FTIR spectra in situ during slow potential scanning of 5 mV s^{-1}. For each spectrum 32 interferograms were co-added covering a range of about 80 mV. The resolution was 4 cm^{-1}. The spectra are related to a reference spectrum, recorded at a potential where no Faradaic reaction occurs. Thus bands pointing upwards are due to the appearance of new features, and bands pointing downwards are related to the disappearance of bands formerly present in the reference.

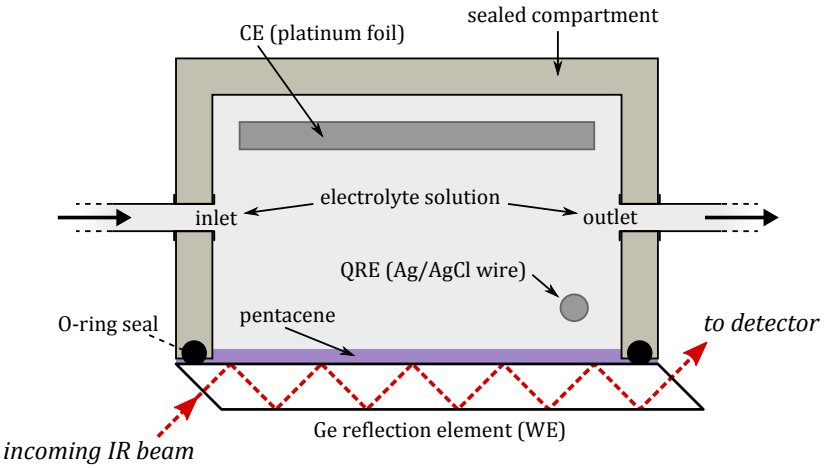

Figure 6.8: Top view illustrating the spectroelectrochemical cell used for FTIR-ATR measurements

In Figure 6.9 the obtained FTIR-ATR difference spectra for pentacene during *p*- and *n*-doping are shown. During *p*-doping the appearance of new infrared bands is observed, with the most pronounced changes between 1500 and 800 cm^{-1}. The peak marked with a star '*' at 845 cm^{-1} is not a feature of the pentacene film, but due to the incorporation of the anion PF_6^- into the film during the doping process.

During *n*-doping most changes are seen in the range between 1600 and 700 cm^{-1}, and the graph area has been restricted to this range for a better comparison of the changes. Strong bands pointing downwards can be seen at 1295 cm^{-1}, 907 cm^{-1} and 730 cm^{-1}, corresponding to the disappearance of distinct infrared bands of the neutral form of the pentacene (see Figure 6.10), where the band at 1295 cm^{-1} corresponds to C-C stretching vibrations, and the latter two correspond to C-H out-of-plane bending modes [64].

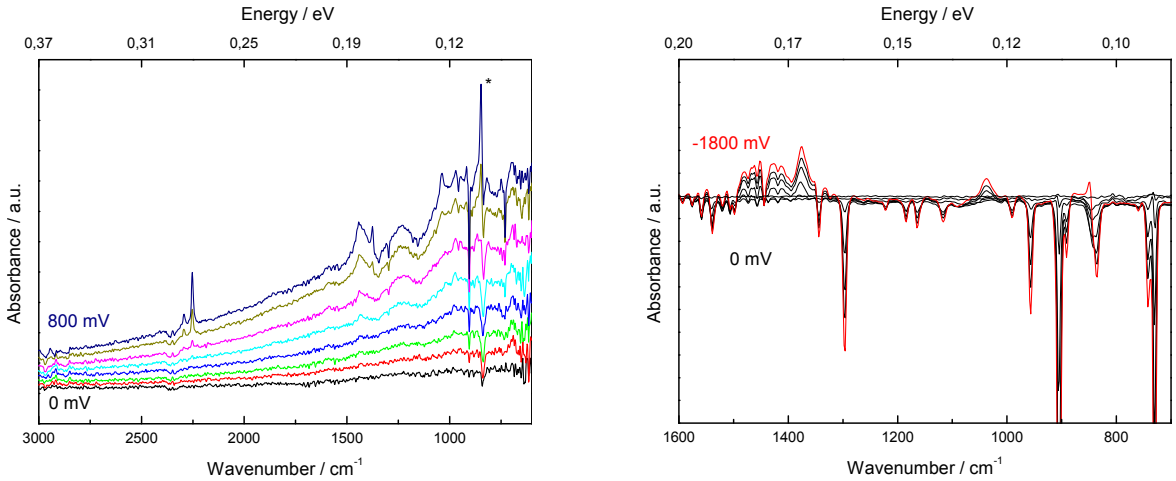

Figure 6.9: FTIR-ATR difference spectra of pentacene during *p*- (left) and *n*-doping (right) recorded at a scan rate of 5 mV s^{-1} in 0.1 M $TBAPF_6$-ACN solution

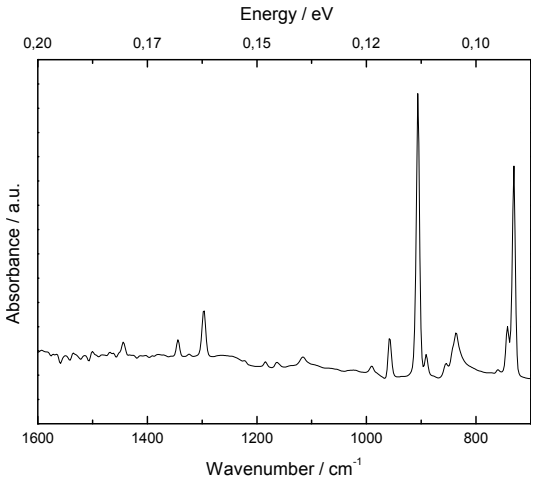

Figure 6.10: FTIR-ATR spectrum of the neutral form of pentacene

7 Electrochemistry for device doping

As shown in the last chapter pentacene can be reversibly *p*- and *n*-doped by electrochemistry. Especially during the *p*-doping the material undergoes drastic changes, as could be seen in the UV-VIS and FTIR-ATR spectra. As pentacene is widely used as a semiconductor material in OFETs, it could be rewarding to investigate the influence of electrochemical doping on the device performance of a transistor, especially the change in contact resistance between the metal source and drain contacts and the semiconductor. Positive effects on the contact resistance by *chemical doping* have been shown in the literature, for example for semiconducting single-walled carbon nanotubes (s-SWNTs) [3] or RR-P3HT (regioregular poly-3-hexylthiophene) and MEH-PPV [poly(2-methoxy-5-(2'-ethyl-hexyloxy)-1,4-phenylene vinylene)] [4].

7.1 Device preparation

As pentacene is known to be a *p*-type semiconductor, the influence of additional positive charge carriers in the material seemed interesting. Supported by the drastic material changes observed by *in-situ* spectroelectrochemistry during oxidation, the focus was put on *p*-doping the material in an OFET device. To improve the contact properties between the metal source and drain contacts and the pentacene, a bottom-gate top-contact OFET was prepared, as described in Chap. 5, where the top Au contacts acted as the working electrodes in the electrochemical setup (see Figure 7.1 for a schematic).

For this purpose indium press-in contacts were used to solder insulated copper wires to the source and drain contacts. The contact areas were then sealed with paraffin wax to prevent dissolution of the indium in the $TBAPF_6$-ACN electrolyte solution, as well as serving as an electric insulator on the contacts. However, the doping process did not work out as planned. As soon as a potential was applied to the contacts while the sample was immersed in the electrolyte solution, the pentacene layer detached from the glass substrate and the aluminum oxide, taking with it the top Au contacts as well. As can be seen in Figure 7.2, only the Al_2O_3 gate contact and the parts of the gold contacts which were covered in paraffin wax remain on the sample.

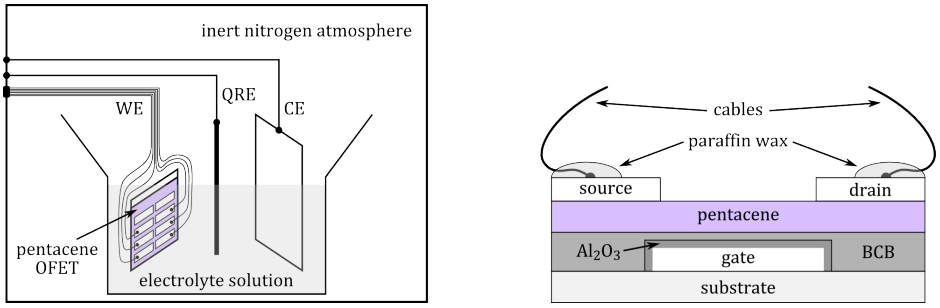

Figure 7.1: Electrochemical setup for OFET doping (left), where the source and drain contacts act as the working electrodes (sideview of an OFET, right)

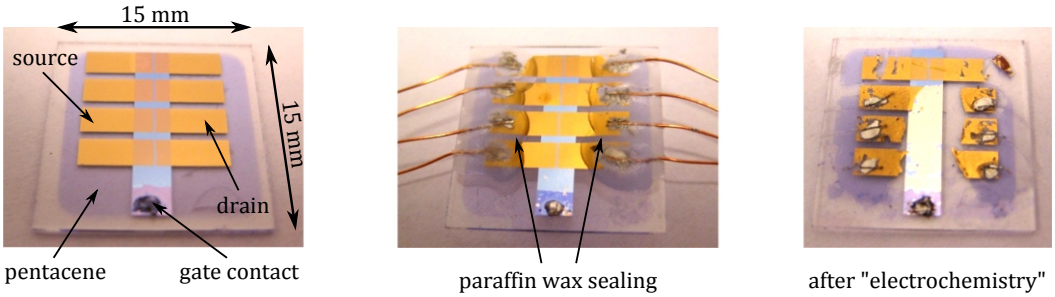

Figure 7.2: Photograph of a bottom-gate top-contact pentacene OFET: as prepared (left); after soldering of insulated Cu cables, where the contact areas are protected by paraffin wax (middle); after applying a potential to three of the source/drain pairs, while the sample was immersed in $TBAPF_6$-ACN, the pentacene detaches (right). Cu cables and paraffin wax were removed for the last picture

No potential had been applied to the source/drain pair farthest from the gate contact, and it can be seen still intact.

To overcome the problem of detachment, a thin layer of PVA was spun on top of the prepared samples before the cables were soldered onto. The PVA acts like a glue, holding together the sample during the doping process. To rule out any effects of this layer on the electrochemistry of the pentacene, the spectroscopic measurements in the UV-VIS and the infrared regime were conducted again, this time with the pentacene covered by the thin PVA film, and the results obtained were identical with the previous measurements performed on the uncovered pentacene. Additionally, Figure 7.3 shows the redox responses for *p*-doping on three different working electrodes, namely pentacene evaporated on a platinum foil and an ITO electrode, as well as on a transistor with a PVA layer on top. The difference in the magnitude of current is mainly due to the different active areas of the electrodes, but the increase in oxidation current around 800 mV is clearly visible in all configurations. Another issue was the possibility of the PVA layer on top influencing the OFET device characteristics. The transfer characteristics of a typical device (40 nm Al_2O_3, BCB interfacial layer, 50 nm pentacene, Au top contacts) be-

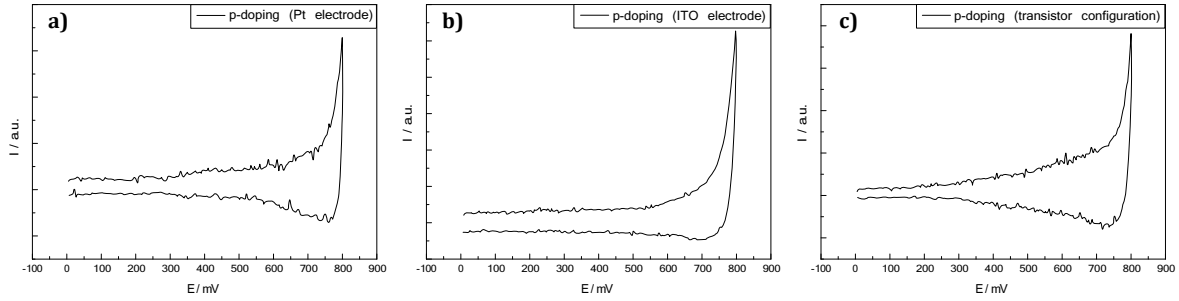

Figure 7.3: Cyclic voltammograms of pentacene oxidation in 0.1 M $TBAPF_6$-ACN, using a) platinum, b) indium tin oxide (ITO) and c) the source/drain contacts of an OFET as working electrode

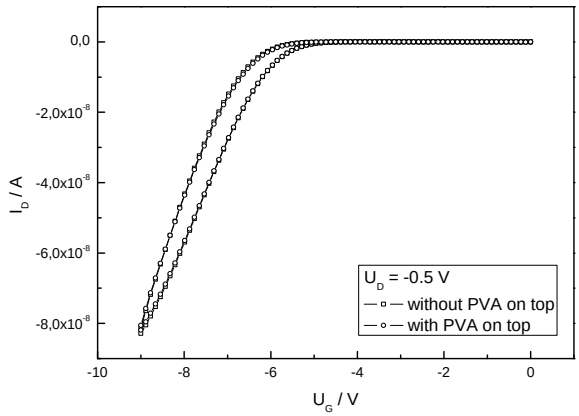

Figure 7.4: Transfer characteristics of a typical pentacene transistor before and after spin-casting a PVA layer on top of the device

fore and after spin-casting the top PVA layer were measured and are shown in Figure 7.4 for a drain voltage of $U_D = -0.5\,\mathrm{V}$. The curves are indistinguishable within the accuracy of the measurement, proofing that the PVA layer has no influence on the device performance.

7.2 Choosing the right settings

Stabilized by the PVA layer devices could be doped using different experimental parameters. After the doping the samples were always flushed gently with acetonitrile solution to get rid of any adsorbed ions on the surface. These do not contribute to the doping process, as they are not incorporated in the film, but might affect the device performance later on when drying the sample, as they form salt crystallites. After flushing, the samples were put into saturated ACN atmosphere inside the glovebox for 30 min to dry.

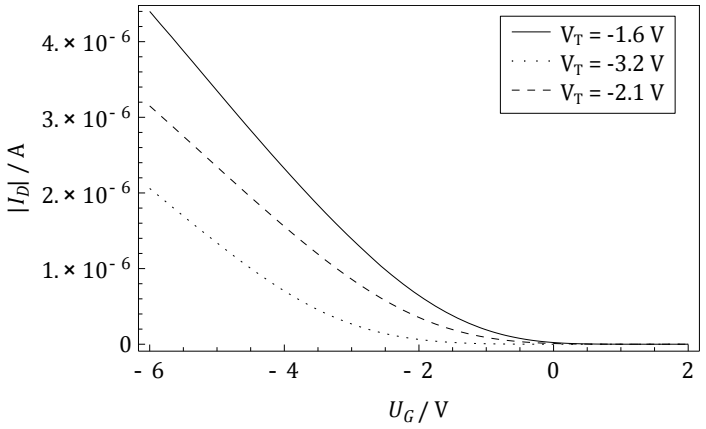

Figure 7.5: Transfer characteristics of a pentacene transistor at $V_D = -2\,\mathrm{V}$, shown for the device as prepared (solid line), after dipping it in electrolyte solution and drying it shortly (dotted line), and after drying the device for longer time (dashed line). The respective threshold voltages are given in the inset, as determined by the SD method

The doping potential was chosen as 800 mV, as the best *p*-doping process could be observed at this value. Going to higher potentials would lead to irreversible changes in the film, as was shown previously in the cyclic voltagram in Figure 6.3. In order to keep the pentacene in its oxidized state, only half-cycle scans of the potential (0–800 mV) were conducted, instead of the full-cycle scans (0–800–0 mV) used for material characterization where the system is brought back to its initial state.

One main problem of this application of electrochemical doping is bringing the transistor in contact with the electrolyte solution. Just dipping a sample into the electrolyte for a few minutes, without applying a potential to the electrodes, worsens the device characteristics, mainly due to a shift of the threshold voltage. This is exemplified in Figure 7.5, where the values of the threshold voltage are given in the inset. The solid line shows the transfer characteristics of the prepared device, already with a PVA layer spun on top. After dipping the sample into 0.1 M $TBAPF_6$-ACN for five minutes, the sample was flushed with acetonitrile and dried for 30 min, as described before, and the transfer characteristics were measured again, represented by the dotted line in Figure 7.5. The value of the on current has decreased by more than a factor of 2, a value observed for many samples. By letting the sample dry for another 60 minutes in the glovebox however it partially recovers (dashed line in the graph), but does not reach the initial value again, even after drying for several days.

By changing the electrolyte solution from 0.1 M to 0.01 M $TBAPF_6$-ACN this degradation effect could be lowered, and the measured decrease in on current for several samples was around a factor of 1.5. While this number can be only a rough averaging, as almost every sample be-

haves slightly different, the trend to less degradation is visible in all samples doped in the diluted electrolyte.

7.3 Doping the device

Half-cycle scans to a potential of 800 mV were conducted in 0.01 M $TBAPF_6$-ACN with scan rates of 10, 50 and 100 mV s^{-1}. The measurements were all performed on the same sample, applying the different scan rates to the first three source/drain pairs and leaving the fourth device as prepared, in order to compare the doped devices to the pristine one. As always the sample was flushed with ACN after doping and dried in saturated atmosphere for 30 min. Figure 7.6 shows the transfer characteristics of the 4 devices, with the solid line representing the transfer curve of the inital device, as prepared. As a reference the dotted line shows the device after dipping it in electrolyte solution for 5 min and drying it for 30 min. The device performance is lowered in all four devices by approximately a factor of 1.5. After the dipping procedure, the sample was again immersed in electrolyte solution and the devices were *p*-doped. After drying for half an hour in ACN atmosphere and another 1 hour open in the glove box, the devices were characterized again, resulting in the dashed transfer curves.

Device a) was doped with a scan rate of 10 mV s^{-1}. As can be seen, the on current after doping approaches almost the value of the inital measurement. A scan rate of 50 mV s^{-1} was applied to device b), leading to an *improvement* of the device characteristics. The on current is higher than the current measured in the initial device. For device c), a scan rate of 100 mV s^{-1} was used, leading to a lower on current than in the initial measurement. However, the current is improved in comparison to the measurement after dipping the sample. Comparing all these results to the undoped fourth device shown in d), which basically just underwent two dipping steps, it can be seen what happens without doping. The second dipping step decreases the on current even further, and the final transfer curve is below the one from the first dipping step. This indicates that even the doping at 100 mV s^{-1} leads to a performance increase compared to no doping at all, but it can not overcome the losses caused by the dipping into the electrolyte solution.

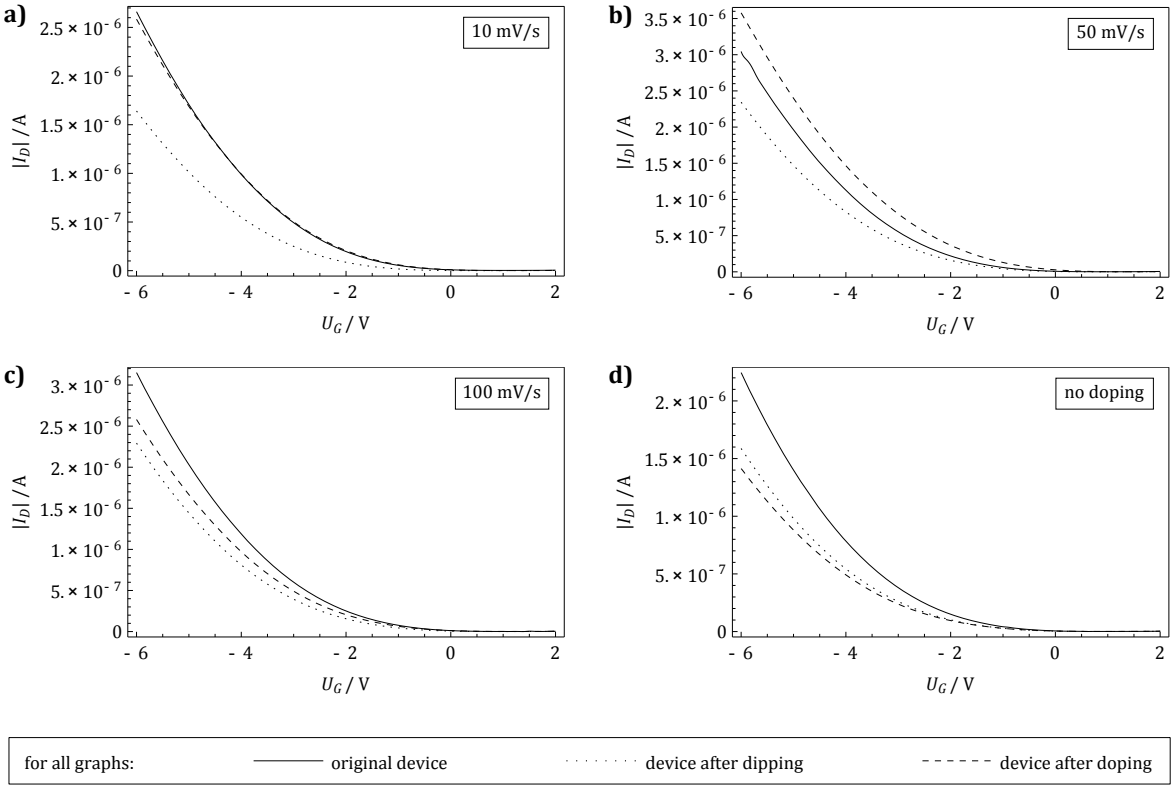

Figure 7.6: Transfer characteristics of 4 devices produced on the same glass substrate, where device a)–c) have been *p*-doped at different scan rates, and device d) was left undoped. For details see text

8 Changes in the contact resistance

To gain a better understanding of the changes in a device induced by electrochemical doping, contact resistance measurements were conducted using the transfer line method (TLM), as described in Sec. 4.3.3. For this purpose 5 transistors with varying channel lengths from 40 to 120 µm were prepared on the same glass substrate, therefore ensuring that all devices were produced with the same material and production properties. The shadow mask used for depositing the source and drain contacts is shown in Figure 5.8.

The transfer and output characteristics of a device with 60 µm channel length on a 80 nm Al_2O_3 - 0.1 wt% BCB - 50 nm pentacene sample are shown in Figure 8.1. The transfer curve was measured in the linear regime, with a drain voltage of $V_D = -0.5\,\mathrm{V}$. An on/off ratio of 1.5×10^4 is observed when sweeping the gate voltage from 0 to $-8\,\mathrm{V}$. The output curves are shown for gate voltages ranging from -3 to $-8\,\mathrm{V}$.

Before the doping procedure, the sample was prepared as described in Chap. 7, with a PVA layer spun ontop and cables soldered to the contacts, covered with paraffin wax. Transfer curves in the linear regime ($V_D = -0.5\,\mathrm{V}$) were recorded for all contacts to obtain the initial value for the contact resistance by using equations (4.12) and (4.13).

As the TLM is very sensitiv to the value of the threshold voltage, this parameter was determined by the second derivative (SD) method, as recommended by Boudinet et al. [37]. The

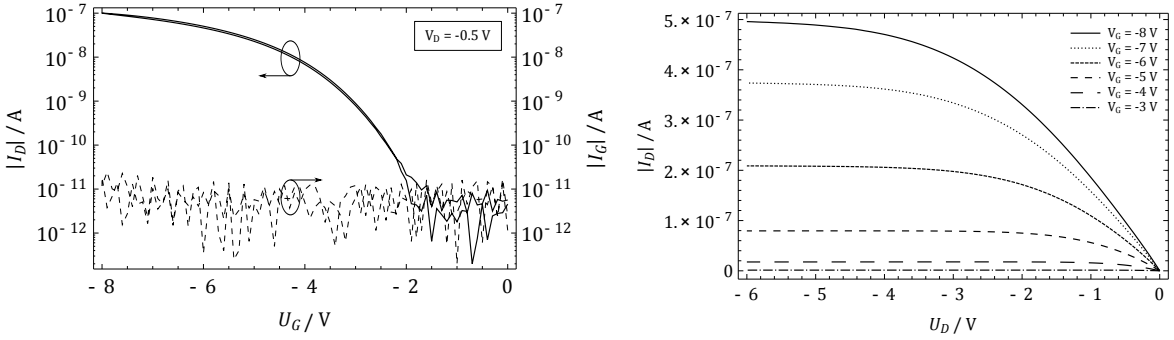

Figure 8.1: Transfer and output characteristics of a pentacene OFET with $L = 60$ µm as used for the TLM measurement. The dashed line in the transfer characteristics corresponds to the leakage current I_G of the device

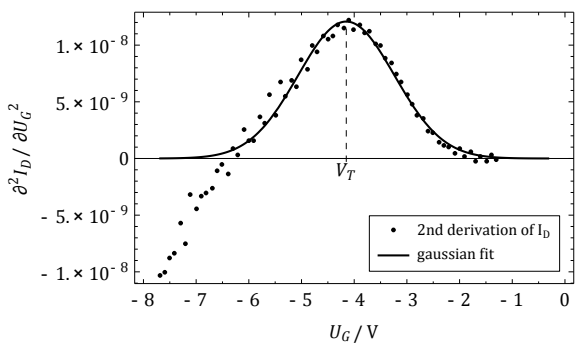

Figure 8.2: Application of the SD method to determine the threshold voltage for the transfer curve shown in Figure 8.1

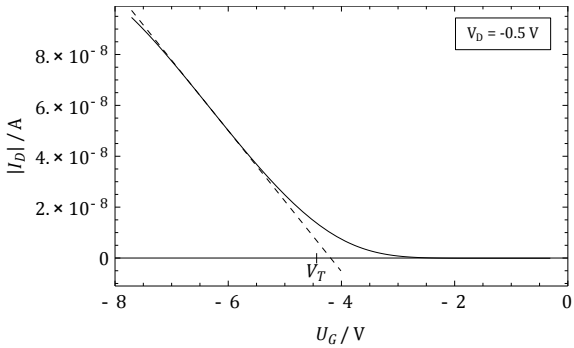

Figure 8.3: The ELR method was deployed for comparison with the SD method, with the dashed line representing the linear extrapolation of the maximum first derivative point

application of this method is shown in Figure 8.2. The transfer curve in the linear regime is numerically differentiated twice, with the data points plotted in the graph as black dots. Then a non-normalized gaussian function is fit to the data points, with the center position representing the maximum value of the second derivative, which equals the threshold voltage. A value of $V_T = -4.2$ V was determined for the shown sample. For comparison also the ELR method is shown in Figure 8.3, as it gives a very descriptive picture of how to estimate the threshold voltage. A value of $V_T = -4.4$ V was obtained with this method. According to Boudinet et al. [37], this slight overestimation of the threshold voltage via the ELR method is expected, and should get worse for decreasing channel length. Therefore the SD method is more trustworthy.

Having obtained the threshold voltage for every device on the sample, the width-normalized resistance as a function of $(V_G - V_T)$ can be calculated, and linear extrapolation to zero channel length yields the contact resistance. Figure 8.4 shows this plot for values of $V_G - V_T = -0.7$ V, -1.2 V, -1.7 V. As expected the contact resistance shows a gate voltage dependence [37, 41]. The doping procedure was then started by first dipping the sample for 5 min into 0.01 M $TBAPF_6$-ACN, afterwards flushing it with pure ACN and drying it in saturated ACN atmosphere for 30 min. Then transfer curves for every contact were again recorded. As contact with the electrolyte solution induces changes in the threshold voltage, as shown before in Sec. 7.2, Figure 7.5, V_T was always reconfirmed by the SD method for every new transfer curve. After drying the sample for 1 more hour open in the glovebox, another set of transfer curves was measured.

Then the sample was again immersed in the electrolyte solution, and all contacts were *p*-doped with a half-cycle scan to 800 mV, at a scan rate of 50 mV s^{-1}, as this setting had shown the most promising results (see Sec. 7.3). The sample was then again flushed with ACN and

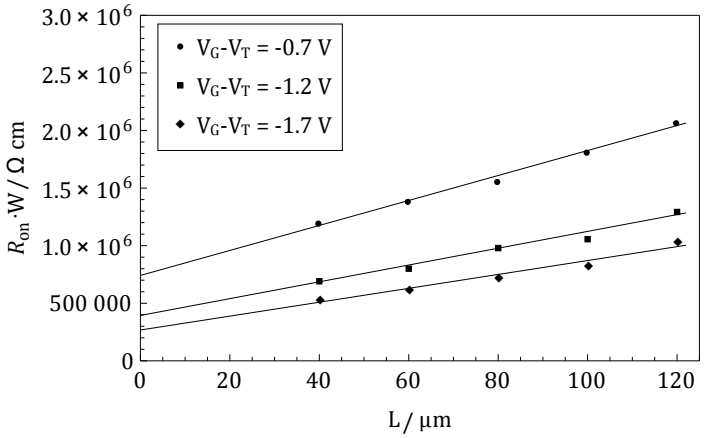

Figure 8.4: TLM measurement for an undoped sample for different values of $V_G - V_T$

dried in ACN atmosphere for 30 min. A contact resistance measurement was then conducted, as well as after 1 hour, 24 hours and 5 days of further drying in the glovebox. The doping steps are summarized in Table 8.1, together with the values obtained for the contact resistance. These values are graphically represented in Figure 8.5. The TLM graphs resulting from the measurements are shown in Figure 8.6.

		$R_c \cdot W\,[\Omega\,\mathrm{cm}]$, for $V_G - V_T =$		
# of TLM measurement		$-0.7\,\mathrm{V}$	$-1.2\,\mathrm{V}$	$-1.7\,\mathrm{V}$
(1)	sample as prepared, with PVA layer spun on top	741516	394165	267639
(2)	after 5 min dipping in electrolyte and 30 min drying	974780	529387	415805
(3)	after drying for one more hour in the glovebox	806047	540625	345023
(4)	after doping the contacts and drying for 30 min	646500	296204	195840
(5)	after drying for one more hour in the glovebox	452284	258870	174455
(6)	after 24 h of drying	331590	193695	142891
(7)	after 5 days of drying	253075	138934	102517

Table 8.1: Overview of the doping procedures and the values obtained for the contact resistance, given in units of Ω cm, for the different values of $V_G - V_T$

As can be seen from the data the contact resistance increases by more than 30 % when the devices are only dipped into the electrolyte (step (1)→(2)). This is in good agreement with the decrease in current shown earlier in Figure 7.5. The contact resistance then gets slightly lower by drying the sample (step (3)). By doping the sample the contact resistance shows a distinct decrease (step (4)), and further improves with the time the sample is dried in inert

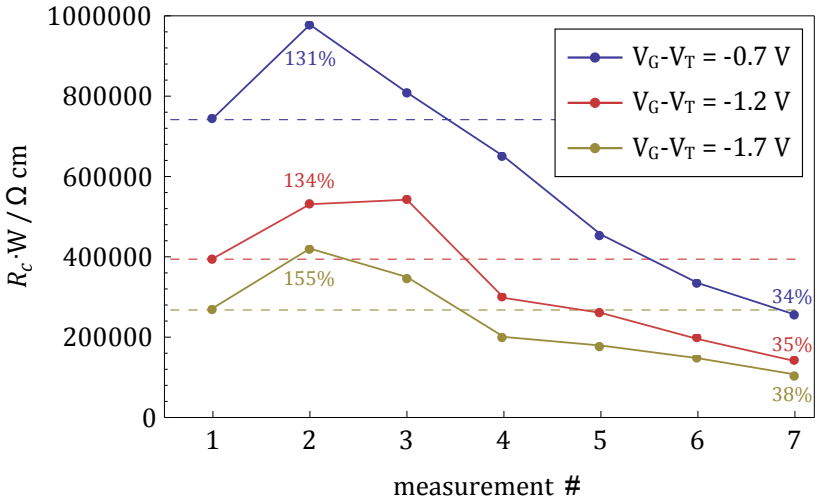

Figure 8.5: Values of the contact resistance for different gate voltages, with the measurement number according to the steps in the doping process (see Table 8.1). The %-values inset relate to the value of step (1)

atmosphere ((5)→(7)). As can be seen in the insets of Figure 8.5, the final value for the contact resistance is more than 60 % lower than the initial value.

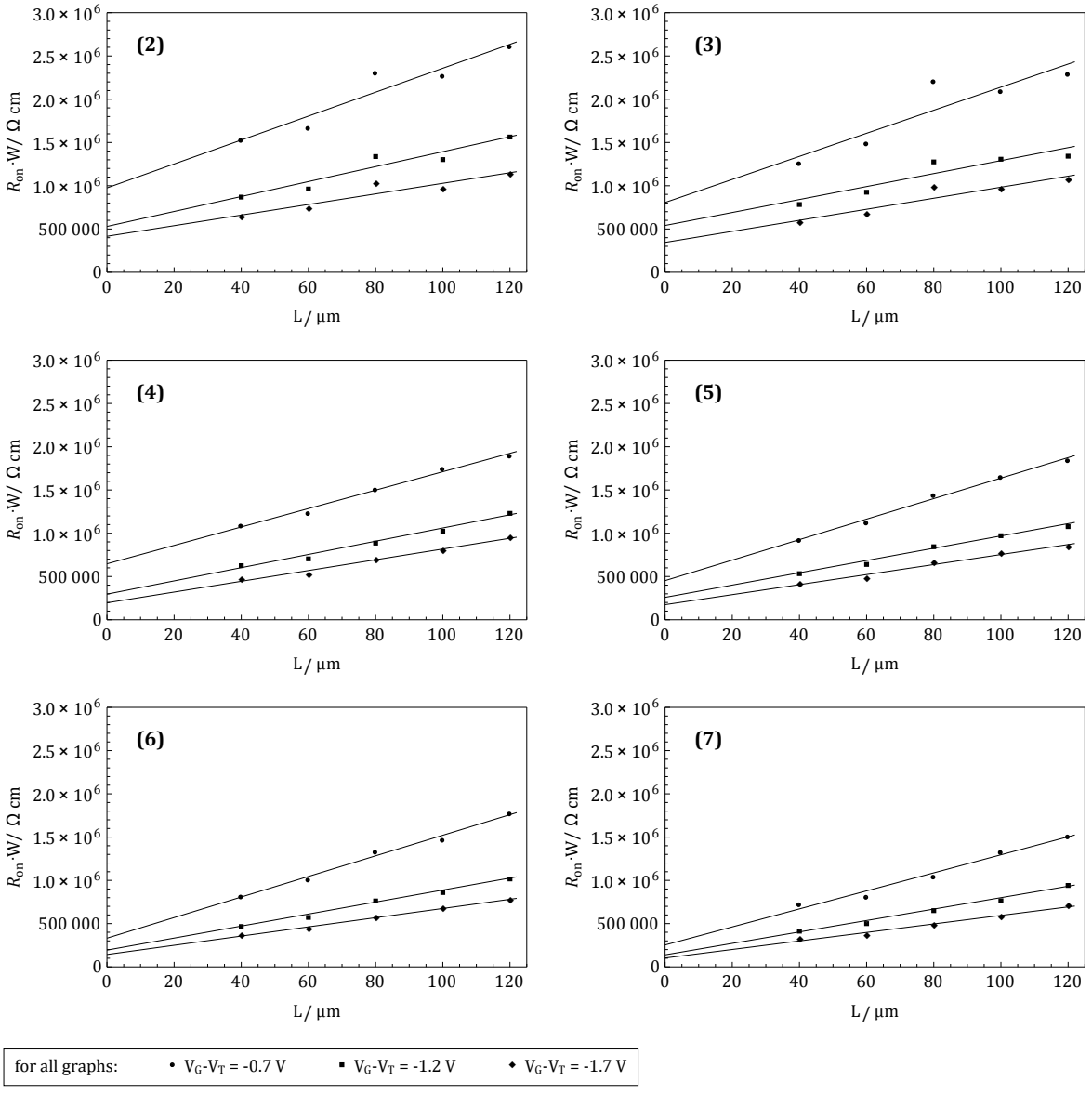

Figure 8.6: TLM measurements taken after each according step in the doping process (Table 8.1)

9 Summary and conclusions

The electrochemical data obtained in chapter 6 showed that pentacene can be reversibly oxidized and reduced. The *in-situ* spectroelectrochemical methods in the UV-visible and the infrared regime however show that the changes during *n* and *p*-doping are clearly different, which might be due to a different effective delocalization along the pentacene molecule.

As pentacene is well known as a *p*-type semiconductor in organic field-effect transistors, the focus of this work was set only on the electrochemical *p*-doping, or oxidation, of the material.

From the EVS measurements, the electrochemical bandgap and the energetic levels, namely HOMO and LUMO, of the pentacene were estimated. The bandgap was found to be 2.2 eV, which is in excellent agreement with values found in the literature [61, and references therein].

Based on the results obtained from CV measurements (Sec. 6.2), a doping potential of 800 mV was chosen, which is above the onset of oxidation and below the potential where irreversible changes happen to the material.

Dipping an OFET into 0.1 M electrolyte solution worsens the device performance drastically, as described in section 7.2. This might be due to a swelling of the pentacene film as a result of intake of electrolyte solution. This is supported by the fact that drying the device for a certain amount of time helps regain the device performance. However also the amount of electrolyte salt dissolved in the solution influences the device performance. Therefore it can not be a problem of swelling alone, but also due to the incorporation of ions into the pentacene film. As the decrease in OFET performance was less pronounced in diluted electrolyte solution, 0.01 M $TBAPF_6$-ACN was used for the doping process.

The doping of the transistors was then conducted by using only half-cycle scans in order to keep the pentacene in its oxidized state. A scan rate of 50 mV s^{-1} was chosen as it yielded the most promising results (Figure 7.6), and measurements of the contact resistance were conducted before and after the doping process.

By selecting the correct parameters for the *p*-doping of pentacene, which are based on the results from electrochemical and spectroelectrochemical measurements, it was shown that the doping of the transistor leads to a decrease in contact resistance, and therefore an improvement of the device performance.

Part III

Appendix

A Anodization of aluminum

An approach to high quality gate insulators for OFET applications are anodized metal films, where an oxide layer is electrochemically grown on the metal surface (see Sec. 5.2 and [46]). This is achieved by galvanostatic anodization, where the metal is immersed in an electrolyte solution equipped with a counterelectrode (see Figure A.1 for a schematic representation of the experimental setup). By controlling the Faraday current through the system, a thin dielectric oxide layer is obtained.

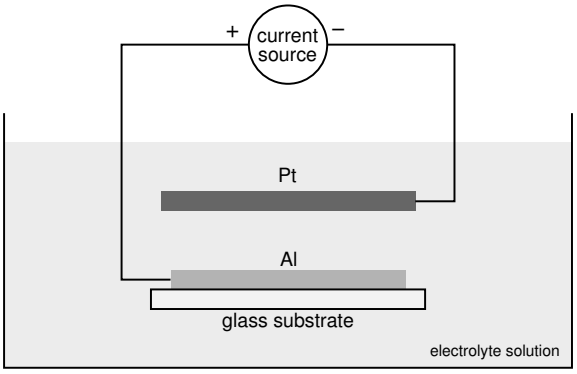

Figure A.1: Schematic of the anodization setup, with an aluminum working electrode and a platinum counter electrode

Platinum serves as a counter electrode, and a thin layer of aluminum on a glass substrate as the working electrode. The preparation is described in Chap. 5. By monitoring the *anodization time* of the galvanostatic process, the *thickness* of the oxide layer is controlled, as is shown in the following.

The oxidation process of aluminum is given by

$$\begin{aligned} \text{anode reaction:} \quad & 2\mathrm{Al} + 3\mathrm{H_2O} \quad \rightarrow \quad \underline{\mathrm{Al_2O_3}} + \underline{6e^-} + 6\mathrm{H^+} \\ \text{cathode reaction:} \quad & 6\mathrm{H^+} + 6e^- \quad \rightarrow \quad 3\mathrm{H_2} \end{aligned}$$

The anode reaction shows that the number of moles of electrons involved is 6 times the one of aluminum oxide molecules: $N_{e^-} = 6 \cdot N_{\mathrm{Al_2O_3}}$. The number of electrons is directly dependent

on the Faraday current I through the electrochemical cell, which is defined by the surface area A times the current density j:

$$I = \frac{Q}{t} = \frac{N_{e^-} \cdot F}{t} \tag{A.1a}$$

$$I = j \cdot A \tag{A.1b}$$

where t denotes the time, and the Faraday constant F is the magnitude of electric charge per mole of electrons ($F = e \cdot N_A$).

Solving equations (A.1a) and (A.1b) for the number of aluminum oxide molecules yields

$$N_{\mathrm{Al_2O_3}} = \frac{N_{e^-}}{6} = \frac{j \cdot A \cdot t}{6 \cdot F} \tag{A.2}$$

As a next step the correlation between the number of moles of aluminum oxide molecules and the thickness $d_{\mathrm{Al_2O_3}}$ of the oxide layer can be derived, where M is the molar mass, ρ the density and V the volume of the material:

$$N_{\mathrm{Al_2O_3}} = \frac{m_{\mathrm{Al_2O_3}}}{M_{\mathrm{Al_2O_3}}} = \frac{\rho_{\mathrm{Al_2O_3}} \cdot V_{\mathrm{Al_2O_3}}}{M_{\mathrm{Al_2O_3}}} = \frac{\rho_{\mathrm{Al_2O_3}} \cdot A \cdot d_{\mathrm{Al_2O_3}}}{M_{\mathrm{Al_2O_3}}} \tag{A.3}$$

Combining equations (A.2) and (A.3) and solving for the oxide thickness results in

$$d_{\mathrm{Al_2O_3}} = \frac{j \cdot M_{\mathrm{Al_2O_3}}}{6 \cdot F \cdot \rho_{\mathrm{Al_2O_3}}} \cdot t \tag{A.4}$$

Using a current density of $j = 0.6\,\mathrm{mA\,cm^{-2}}$ and the numerical values taken from the 'Handbook of Chemistry and Physics' [48], the final formula for aluminum anodization reads

$$d_{\mathrm{Al_2O_3}}\,[\mathrm{nm}] = 0.266\,[\mathrm{nm/s}] \cdot t\,[\mathrm{s}] \tag{A.5}$$

constant	value	unit
j	0.60	$\mathrm{mA\,cm^{-2}}$
$M_{\mathrm{Al_2O_3}}$	101.96	$\mathrm{g\,mol^{-1}}$
F	96 485.34	$\mathrm{C\,mol^{-1}}$
$\rho_{\mathrm{Al_2O_3}}$	3.97	$\mathrm{g\,cm^{-3}}$

B List of abbreviations

ACN ..... acetonitrile
BCB ..... divinyltetramethyldisiloxane-bis(benzo-cyclobutene)
CE ..... counter electrode
CV ..... cyclic voltammetry
ELR ..... extrapolation in the linear region [method]
EVS ..... electrochemical voltage spectroscopy
FET ..... field-effect transistor
FTIR-ATR ..... fourier-transform infrared-attenuated total reflection [spectroscopy]
HOMO ..... highest occupied molecular orbital
I_D ..... drain current
I_G ..... gate (leakage) current
ITO ..... indium tin oxide
LUMO ..... lowest unoccupied molecular orbital
MOSFET ..... metal-oxide-semiconductor field-effect transistor
OFET ..... organic field-effect transistor
PVA ..... polyvinyl alcohol
QRE ..... quasi-reference electrode
RE ..... reference electrode
RM ..... ratio method
SD ..... second derivative [method]
$TBAPF_6$ ..... tetrabutylammonium hexafluorophosphate
TLM ..... transfer line method
UV-VIS ..... UV-visible [spectroscopy]
V_D ..... drain voltage
V_G ..... gate voltage
V_T ..... threshold voltage
WE ..... working electrode

Bibliography

[1] T. B. Singh, P. Senkarabacak, N. S. Sariciftci, A. Tanda, C. Lackner, R. Hagelauer, and G. Horowitz. Organic inverter circuits employing ambipolar pentacene field-effect transistors. *Applied Physics Letters*, 89: 033512. doi:10.1063/1.2235947

[2] R. Schmechel, M. Ahles, and H. von Seggern. A pentacene ambipolar transistor: Experiment and theory. *Journal of Applied Physics*, 98: 084511. doi:10.1063/1.2106009

[3] T. Kanbara, T. Takenobu, T. Takahashi, Y. Iwasa, K. Tsukagoshi, Y. Aoyagi, and H. Kataura. Contact resistance modulation in carbon nanotube devices investigated by four-probe experiments. *Applied Physics Letters*, 88: 053118. doi:10.1063/1.2171481

[4] Y. Chen, I. Shih, and S. Xiao. Effects of $FeCl_3$ doping on polymer-based thin film transistors. *Journal of Applied Physics*, 96: (2004), 454–458. doi:10.1063/1.1760838

[5] A. J. Heeger, S. Kivelson, J. R. Schrieffer, and W. P. Su. Solitons in conducting polymers. *Rev. Mod. Phys.*, 60: (1988), 781–850. doi:10.1103/RevModPhys.60.781

[6] Z. Bao and J. Locklin, editors. *Organic Field-Effect Transistors*. CRC Press, 2007

[7] O. Piringer and A. L. Baner, editors. *Plastic Packaging*. Wiley-VCH, Weinheim, 2nd edition, 2008

[8] R. E. Peierls. *Quantum Theory of Solids*. Oxford University Press, 1955

[9] R. Comès, M. Lambert, H. Launois, and H. R. Zeller. Evidence for a Peierls Distortion or a Kohn Anomaly in One-Dimensional Conductors of the Type $K_2Pt(CN)_4Br_{0.30} \cdot xH_2O$. *Phys. Rev. B*, 8: (1973), 571–575. doi:10.1103/PhysRevB.8.571

[10] J. E. Anthony, J. S. Brooks, D. L. Eaton, and S. R. Parkin. Functionalized Pentacene: Improved Electronic Properties from Control of Solid-State Order. *Journal of the American Chemical Society*, 123: (2001), 9482–9483. doi:10.1021/ja0162459

[11] D. D. Eley. Phthalocyanines as Semiconductors. *Nature*, 162: (1948), 819–819. doi: 10.1038/162819a0

[12] D. A. Neamen. *Semiconductor Physics And Devices*. McGraw-Hill, Inc., New York, NY, USA, 3rd edition, 2003

[13] N. Karl, J. Marktanner, R. Stehle, and W. Warta. High-field saturation of charge carrier drift velocities in ultrapurified organic photoconductors. *Synthetic Metals*, 42: (1991), 2473 – 2481. doi:10.1016/0379-6779(91)91407-2

[14] A. J. Heeger. Semiconducting and Metallic Polymers: The Fourth Generation of Polymeric Materials. *J. Phys. Chem. B*, 105: (2001), 8475–8491. doi:10.1021/jp011611w

[15] G. Horowitz, R. Hajlaoui, and P. Delannoy. Temperature Dependence of the Field-Effect Mobility of Sexithiophene. Determination of the Density of Traps. *J. Phys. III France*, 5: (1995), 355–371. doi:10.1051/jp3:1995132

[16] M. C. J. M. Vissenberg and M. Matters. Theory of the field-effect mobility in amorphous organic transistors. *Phys. Rev. B*, 57: (1998), 12964–12967. doi:10.1103/PhysRevB.57.12964

[17] A. Miller and E. Abrahams. Impurity Conduction at Low Concentrations. *Phys. Rev.*, 120: (1960), 745–755. doi:10.1103/PhysRev.120.745

[18] N. F. Mott. Nobel Lecture. Nobelprize.org, http://nobelprize.org/nobel_prizes/physics/laureates/1977/mott-lecture.html, December 8, 1977

[19] H. Shirakawa, E. J. Louis, A. G. MacDiarmid, C. K. Chiang, and A. J. Heeger. Synthesis of electrically conducting organic polymers: halogen derivatives of polyacetylene, $(CH)_x$. *J. Chem. Soc. Chem. Commun.*, page 578. doi:10.1039/C39770000578

[20] C. K. Chiang, C. R. Fincher, Y. W. Park, A. J. Heeger, H. Shirakawa, E. J. Louis, S. C. Gau, and A. G. MacDiarmid. Electrical Conductivity in Doped Polyacetylene. *Phys. Rev. Lett.*, 39: (1977), 1098–1101. doi:10.1103/PhysRevLett.39.1098

[21] K. Izutsu. *Electrochemistry in Nonaqueous Solutions*. Wiley-VCH, 2002. doi:10.1002/3527600655

[22] Southampton Electrochemistry Group. *Instrumental methods in electrochemistry*. Horwood Publishing, 2001

[23] C. Kvarnström, A. Ivaska, and H. Neugebauer. *Advanced Functional Molecules and Polymers*, volume 2, chapter 6, pages 139–169. 2001

[24] J. Lilienfeld. US Patent 1745175. 1930. Method and apparatus for controlling electric currents

[25] *D. Kahng, M. M. Atalla, IRE Solid-State Devices Research Conference, Carnegie Institute of Technology, Pittsburgh, PA*. 1960

[26] *P. K. Weimer, Proc. IRE 1962, 50, 1462*

[27] M. Shur. *Physics of Semiconductor Devices*. Prentice-Hall, Englewood Cliffs, NJ, 1990

[28] A. Tsumura, H. Koezuka, and T. Ando. Macromolecular electronic device: Field-effect transistor with a polythiophene thin film. *Applied Physics Letters*, 49: (1986), 1210–1212. doi:10.1063/1.97417

[29] G. Horowitz. Organic Field-Effect Transistors. *Advanced Materials*, 10: (1998), 365–377. doi:10.1002/(SICI)1521-4095(199803)10:5<365::AID-ADMA365>3.0.CO;2-U

[30] H. Klauk, M. Halik, U. Zschieschang, G. Schmid, W. Radlik, and W. Weber. High-mobility polymer gate dielectric pentacene thin film transistors. *Journal of Applied Physics*, 92: (2002), 5259–5263. doi:10.1063/1.1511826

[31] H. Klauk, editor. *Organic Electronics*. Wiley-VCH, 2006

[32] M. Halik, H. Klauk, U. Zschieschang, G. Schmid, C. Dehm, M. Schütz, S. Maisch, F. Effenberger, M. Brunnbauer, and F. Stellacci. Low-voltage organic transistors with an amorphous molecular gate dielectric. *Nature*, 431: (2004), 963–966. doi:10.1038/nature02987

[33] T. Someya, T. Sekitani, S. Iba, Y. Kato, H. Kawaguchi, and T. Sakurai. A large-area, flexible pressure sensor matrix with organic field-effect transistors for artificial skin applications. *Proceedings of the National Academy of Sciences of the United States of America*, 101: (2004), 9966–9970. doi:10.1073/pnas.0401918101

[34] T. Takenobu, T. Takahashi, T. Kanbara, K. Tsukagoshi, Y. Aoyagi, and Y. Iwasa. High-performance transparent flexible transistors using carbon nanotube films. *Applied Physics Letters*, 88: 033511. doi:10.1063/1.2166693

[35] H. B. Michaelson. The work function of the elements and its periodicity. *Journal of Applied Physics*, 48: (1977), 4729–4733. doi:10.1063/1.323539

[36] M. Mottaghi and G. Horowitz. Field-induced mobility degradation in pentacene thin-film transistors. *Organic Electronics*, 7: (2006), 528 – 536. ISSN 1566-1199. doi:10.1016/j.orgel.2006.07.011

[37] D. Boudinet, G. L. Blevennec, C. Serbutoviez, J.-M. Verilhac, H. Yan, and G. Horowitz. Contact resistance and threshold voltage extraction in n-channel organic thin film transistors on plastic substrates. *Journal of Applied Physics*, 105: 084510. doi:10.1063/1.3110021

[38] H.-S. Wong, M. H. White, T. J. Krutsick, and R. V. Booth. Modeling of transconductance degradation and extraction of threshold voltage in thin oxide MOSFET's. *Solid-State Electronics*, 30: (1987), 953 – 968. doi:10.1016/0038-1101(87)90132-8

[39] D. Boudinet, M. Benwadih, Y. Qi, S. Altazin, J.-M. Verilhac, M. Kroger, C. Serbutoviez, R. Gwoziecki, R. Coppard, G. L. Blevennec, A. Kahn, and G. Horowitz. Modification of gold source and drain electrodes by self-assembled monolayer in staggered n- and p-channel organic thin film transistors. *Organic Electronics*, 11: (2010), 227 – 237. doi:10.1016/j.orgel.2009.10.021

[40] B. Stadlober, U. Haas, H. Gold, A. Haase, G. Jakopic, G. Leising, N. Koch, S. Rentenberger, and E. Zojer. Orders-of-Magnitude Reduction of the Contact Resistance in Short-Channel Hot Embossed Organic Thin Film Transistors by Oxidative Treatment of Au-Electrodes. *Advanced Functional Materials*, 17: (2007), 2687–2692. doi:10.1002/adfm.200700294

[41] S. Luan and G. W. Neudeck. An experimental study of the source/drain parasitic resistance effects in amorphous silicon thin film transistors. *Journal of Applied Physics*, 72: (1992), 766–772. doi:10.1063/1.351809

[42] R. J. Chesterfield, J. C. McKeen, C. R. Newman, C. D. Frisbie, P. C. Ewbank, K. R. Mann, and L. L. Miller. Variable temperature film and contact resistance measurements on operating n-channel organic thin film transistors. *Journal of Applied Physics*, 95: (2004), 6396–6405. doi:10.1063/1.1710729

[43] K. P. Puntambekar, P. V. Pesavento, and C. D. Frisbie. Surface potential profiling and contact resistance measurements on operating pentacene thin-film transistors by Kelvin probe force microscopy. *Applied Physics Letters*, 83: (2003), 5539–5541. doi:10.1063/1.1637443

[44] P. Marmont, N. Battaglini, P. Lang, G. Horowitz, J. Hwang, A. Kahn, C. Amato, and P. Calas. Improving charge injection in organic thin-film transistors with thiol-based self-assembled monolayers. *Organic Electronics*, 9: (2008), 419 – 424. doi:10.1016/j.orgel.2008.01.004

[45] L. A. Majewski, M. Grell, S. D. Ogier, and J. Veres. A novel gate insulator for flexible electronics. *Organic Electronics*, 4: (2003), 27 – 32. doi:10.1016/S1566-1199(03)00005-3

[46] L. Majewski, R. Schroeder, and M. Grell. One Volt Organic Transistor. *Advanced Materials*, 17: (2005), 192–196. doi:10.1002/adma.200400809

[47] J. W. Diggle, T. C. Downie, and C. W. Goulding. Anodic oxide films on aluminum. *Chemical Reviews*, 69: (1969), 365–405. doi:10.1021/cr60259a005

[48] D. R. Lide, editor. *CRC Handbook of Chemistry and Physics*. CRC Press, 82nd edition, 2001

[49] P. Stadler, A. M. Track, M. Ullah, H. Sitter, G. J. Matt, G. Koller, T. B. Singh, H. Neugebauer, N. S. Sariciftci, and M. G. Ramsey. The role of the dielectric interface in organic transistors: A combined device and photoemission study. *Organic Electronics*, 11: (2010), 207 – 211. doi:10.1016/j.orgel.2009.10.017

[50] W. Kalb, P. Lang, M. Mottaghi, H. Aubin, G. Horowitz, and M. Wuttig. Structure-performance relationship in pentacene/Al2O3 thin-film transistors. *Synthetic Metals*, 146: (2004), 279 – 282. doi:10.1016/j.synthmet.2004.08.018

[51] M. Egginger, M. Irimia-Vladu, R. Schwödiauer, A. Tanda, I. Frischauf, S. Bauer, and N. S. Sariciftci. Mobile Ionic Impurities in Poly(vinyl alcohol) Gate Dielectric: Possible Source of the Hysteresis in Organic Field-Effect Transistors. *Advanced Materials*, 20: (2008), 1018–1022. doi:10.1002/adma.200701479

[52] L.-L. Chua, J. Zaumseil, J.-F. Chang, E. C.-W. Ou, P. K.-H. Ho, H. Sirringhaus, and R. H. Friend. General observation of n-type field-effect behaviour in organic semiconductors. *Nature*, 434: (2005), 194–199. doi:10.1038/nature03376

[53] X.-H. Zhang and B. Kippelen. Low-voltage C_{60} organic field-effect transistors with high mobility and low contact resistance. *Applied Physics Letters*, 93: 133305. doi:10.1063/1.2993349

[54] The Dow Chemical Company. CYCLOTENE Advanced Electronics Resins. http://www.dow.com/cyclotene/solution/elecprop.htm

[55] M. Bendikov, H. M. Duong, K. Starkey, K. N. Houk, E. A. Carter, and F. Wudl. Oligoacenes: Theoretical Prediction of Open-Shell Singlet Diradical Ground States. *Journal of the American Chemical Society*, 126: (2004), 7416–7417. doi:10.1021/ja048919w

[56] R. B. Campbell, J. M. Robertson, and J. Trotter. The crystal and molecular structure of pentacene. *Acta Crystallographica*, 14: (1961), 705–711. doi:10.1107/S0365110X61002163

[57] H. Klauk, M. Halik, U. Zschieschang, G. Schmid, W. Radlik, and W. Weber. High-mobility polymer gate dielectric pentacene thin film transistors. *Journal of Applied Physics*, 92: (2002), 5259–5263. doi:10.1063/1.1511826

[58] L. Gross, F. Mohn, N. Moll, P. Liljeroth, and G. Meyer. The Chemical Structure of a Molecule Resolved by Atomic Force Microscopy. *Science*, 325: (2009), 1110–1114. doi:10.1126/science.1176210

[59] A. Kahn, N. Koch, and W. Gao. Electronic structure and electrical properties of interfaces between metals and pi-conjugated molecular films. *Journal of Polymer Science Part B: Polymer Physics*, 41: (2003), 2529–2548. doi:10.1002/polb.10642

[60] A. H. Thompson. Lithium Ordering in Li_xTiS_2. *Phys. Rev. Lett.*, 40: (1978), 1511–1514. doi:10.1103/PhysRevLett.40.1511

[61] C. Baldacchini, C. Mariani, M. G. Betti, L. Gavioli, M. Fanetti, and M. Sancrotti. Molecular gap and energy level diagram for pentacene adsorbed on filled d-band metal surfaces. *Applied Physics Letters*, 89: 152119. doi:10.1063/1.2359573

[62] E. Kötz, H. Neff, and K. Müller. A UPS, XPS and work function study of emersed silver, platinum and gold electrodes. *Journal of Electroanalytical Chemistry*, 215: (1986), 331–344. doi:10.1016/0022-0728(86)87026-7

[63] M. Brinkmann, S. Graff, C. Straupe, J.-C. Wittmann, C. Chaumont, F. Nuesch, A. Aziz, M. Schaer, and L. Zuppiroli. Orienting Tetracene and Pentacene Thin Films onto Friction-Transferred Poly(tetrafluoroethylene) Substrate. *Journal of Physical Chemistry B*, 107: (2003), 10531–10539. doi:10.1021/jp030217q

[64] J. Szczepanski, C. Wehlburg, and M. Vala. Vibrational and electronic spectra of matrix-isolated pentacene cations and anions. *Chemical Physics Letters*, 232: (1995), 221 – 228. doi:10.1016/0009-2614(94)01340-2